Physicochemical processes in the indirect interaction between surface air plasma and

deionized water

Physicochemical processes in the indirect interaction between surface air plasma and deionized water

Z C Liu[1]**, D X Liu**[1]**, C Chen**[1]**, D Li**[1]**, A J Yang**[1]**, M Z Rong**[1]**, H L Chen**[2] **and M G Kong**[1,2,3]

[1] State Key Laboratory of Electrical Insulation and Power Equipment, Center for Plasma Biomedicine, Xi'an Jiaotong University, Xi'an City 710049, People's Republic of China
[2] Frank Reidy Center for Bioelectrics, Old Dominion University, Norfolk, VA 23508, USA
[3] Department of Electrical and Computer Engineering, Old Dominion University, Norfolk, VA 23529, USA

E-mail: liudingxin@mail.xjtu.edu.cn and mglin5g@gmail.com

Abstract

One of the most central scientific questions for plasma applications in healthcare and environmental remediation is the chemical identity and the dose profile of plasma-induced reactive oxygen and nitrogen species (ROS/RNS) that can act on an object inside a liquid. A logical focus is on aqueous physicochemical processes near a sample with a direct link to their upstream gaseous processes in the plasma region and a separation gap from the liquid bulk. Here, a system-level modeling framework is developed for indirect interactions of surface air plasma and a deionized water bulk and its predictions are found to be in good agreement with the measurement of gas-phase ozone and aqueous long-living ROS/RNS concentrations. The plasma region is described with a global model, whereas the air gap and the liquid region are simulated with a 1D fluid model. All three regions are treated as one integrated entity and computed simultaneously. With experimental validation, the system-level modeling shows that the dominant aqueous ROS/RNS are long-living species (e.g. H_2O_{2aq}, O_{3aq}, nitrite/nitrate, H^+_{aq}). While most short-living gaseous species could hardly survive their passage to the liquid, aqueous short-living ROS/RNS are generated *in situ* through reactions among long-living plasma species and with water molecules. This plasma-mediated remote production of aqueous ROS/RNS is important for the abundance of aqueous HO_{2aq}, HO_{3aq}, OH_{aq} and O^-_{2aq} as well as NO_{2aq} and NO_{3aq}. Aqueous plasma chemistry offers a novel and significant pathway to activate a given biological outcome, as exemplified here for bacterial deactivation in plasma-activated water. Additional factors that may synergistically broaden the usefulness of aqueous plasma chemistry include an electric field by aqueous ions and liquid acidification. The system-modeling framework will be useful in assisting designs and analyses of future investigations of plasma-liquid and plasma–cell interactions.

Keywords: surface microdischarge, mass transfer, penetration, reactive oxygen species, reactive nitrogen species, liquid-phase chemistry

(Some figures may appear in colour only in the online journal)

1. Introduction

Cold atmospheric-pressure plasma (CAP) holds great prospects in diverse fields of societal importance such as environmental protection, biomedicine, nanotechnology, and agriculture [1–6]. For many of these applications, the targets of plasma treatment are placed in a humid environment, thus subjecting gaseous plasma species to strong interactions with

water molecules before their arrival at and reaction with the targets. Little is currently known of such complex interactions at a molecular level and many questions remain open. For example, how are the plasma species transferred through the gas/liquid interface and into the liquid bulk, which reactions dominate the passage of gaseous plasma species through the liquid bulk, how deep can the plasma species penetrate into the liquid layer, and what are the dominant plasma species that can actually reach and act on the intended targets? While some of these questions have been addressed usually qualitatively for established applications of plasma-liquid interactions (e.g. wastewater treatment), emerging applications demand quantitative answers. For example, the plasma dose for cancer therapy must be quantitatively appropriate for damaging tumor without affecting healthy tissues and the tolerance for error must be minimal.

While studies of plasma-liquid interactions date back some 120 years ago [7], it is only in recent years when their microscopic processes started to attract interest from the scientific community. For example, it is suggested that electron bombardment on the liquid interface may lead to electrolysis [8] and that ion bombardment onto the liquid could be an important source for the generation of OH_{aq} and H_2O_{2aq} [9]. The strength of new understanding from these and other studies [10] appears to hinge on the plasma-liquid interfacial layer, where many fast-changing physicochemical processes take place simultaneously. Mass transfer across the gas–liquid boundary is coupled to steep and dynamic changes in physical fields of space charges, temperature gradients, and shockwaves. This is further complicated by the chemical reactions of several hundred plasma species. Upon impinging onto liquid, highly reactive plasma species (e.g. hydroxyl radicals) can become quenched within a short distance of hundreds of nanometers and electrons induce aqueous impact reactions within nano seconds, suggesting that changes in the physicochemical properties of the interfacial layer may be confined within a narrow boundary layer of a few micrometers at most. This poses a formidable diagnostic challenge and highlights a knowledge gap of plasma transport and reaction coefficients.

The central objective of a basic understanding of the above phenomena and others is the chemical identities and concentrations of aqueous species at the sample point. Given the short lifetime of charged species ($<100\ \mu$s), being much smaller than the diffusion timescale (~1 s) in atmospheric air, it is not clear how much rapidly changing physicochemical events in the plasma region actually dictate downstream aqueous chemistry. A recent study of the direct interaction of low-power helium plasma with deionized water demonstrates that the topmost layer (close to the gas region) of the liquid bulk acts as a filter to dampen the impact of gas-phase and interfacial phenomena [16]. Given this, an appropriate approach with the current knowledge seems to focus on physicochemical processes near the sample point in liquid but linked to their upstream processes in the gas and plasma-generation regions. The simultaneous treatment of the three cascaded regions of plasma generation, gas gap, and liquid bulk seeks an overall understanding of the landscape of plasma-liquid interactions, to which more detailed and subtle features of relevant

processes may be added from future studies. Numerical models of gas plasma in contact with water have been reported for physicochemical processes in the plasma [8, 11–14] and through the plasma-liquid interface [15–21]. However, rarely has a detailed simulation study of plasma-liquid interactions been supported with experimental validation, even though measurements have been reported of concentrations of liquid-phase ROS/RNS [20]. It is therefore timely to undertake a system-level study of physicochemical processes from the plasma generation region to the liquid bulk, particularly when supported with appropriate liquid-phase measurements.

Direct concentration measurements of liquid-phase species are reported for plasma-activated water (PAW). For example, long-living aqueous plasma species, such as H_2O_{2aq}, nitrite ($NO_{2\,aq}^-$/HNO_{2aq}), and nitrate ($NO_{3\,aq}^-$/HNO_{3aq}), were measured with spectrophotometry and high-performance liquid chromatography [22, 23], whereas short-living species such as OH_{aq}, $O_{2\,aq}^-$, $ONOOH_{aq}$, and NO_{aq} were measured by means of electron spin resonance (ESR) [24, 25]. Some of these studies suggest that H_{aq}^+, H_2O_{2aq}, nitrate and nitrite are the main reactive species in PAW [26], whereas others propose O_{3aq} as key to microbial deactivation [27]. Also, the existence of $ONOOH_{aq}$ is not fully supported [22]. When aqueous plasma species are related to biological effects, there is evidence that plasma-activated water has greater bactericidal capacity than solution containing only nitrite, nitrate and H_2O_{2aq} of similar concentrations at similar pH value [28, 29]. These seemingly contradictory findings could be due to the different plasma doses used in the different studies and could be reconciled when a quantitative model of relevant physicochemical processes becomes available.

Most numerical studies reported so far are based on 0D global description [18–20], and these have been extended very recently to 1D and 2D studies of plasma species penetration in liquid [15, 16] though with little support of experimental data. Predictions of the latter may be validated experimentally with colorimetric measurements of ROS [30–32]. Yet an integrated model depends critically on how plasma interacts with liquid, as it affects how the mass transfer of plasma species through the interfacial layer [1–5, 20, 24, 34–36] is modeled. In this context, we note that atmospheric plasma may be divided depending on whether its charged species are flown onto the liquid surface thus making the liquid part of the electric circuit of the plasma. When the liquid is part of the electric circuit, the plasma directly interacts with the liquid thus inducing strong macroscopic physical fields as detailed in figure 1. These include surface tension and turbulence, and require a 3D description. Common CAP sources with direct liquid interactions include floating-electrode dielectric-barrier discharges [15, 18, 29] and some types of plasma jets [19, 25, 31] and jet arrays [37, 38]. For medical applications, significant macroscopic events such as turbulence are undesirable if they are not quantitatively reproducible for different patients or different medical devices. By contrast, dominant physical processes in indirect plasma-liquid interactions cause little macroscopic disturbance to the liquid surface and are preferred for manipulating cell functions as a basis of cell therapies [21, 22]. Indirect plasma-liquid interactions can be modeled one-dimensionally.
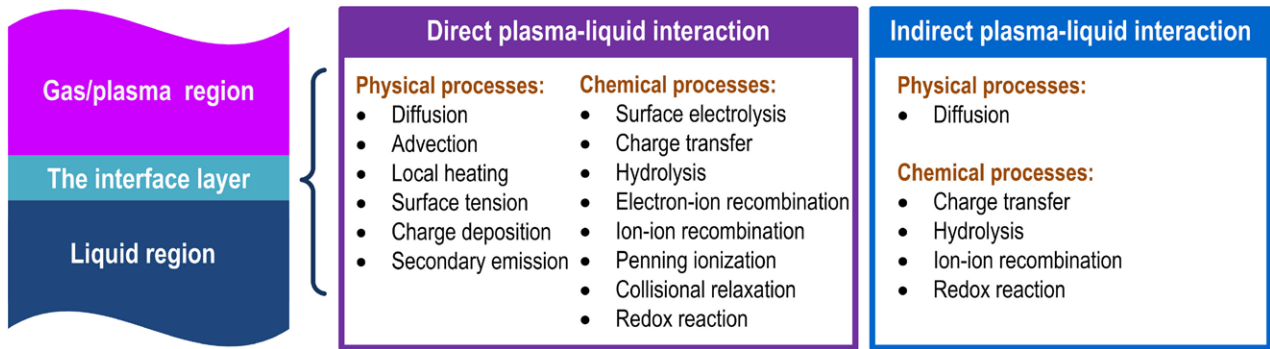
Figure 1. Comparison of direct and indirect plasma-liquid interactions, of which liquid is not part of the electric circuit in indirect interactions.
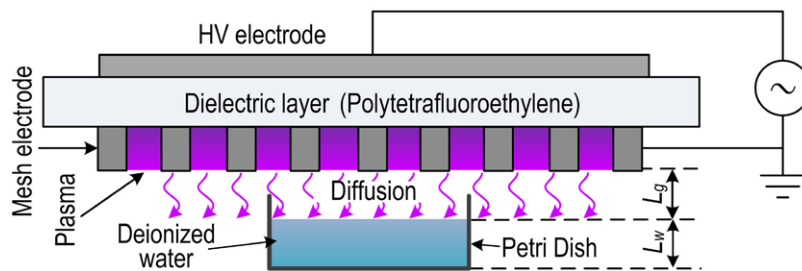
Figure 2. Schematic of the experimental setup.

Indirect plasma-liquid interactions are common with surface plasma [20, 27, 35], so we consider an air surface microdischarge (SMD) with a physically static layer of deionized water as the plasma-treated solution. SMD is essentially an array of surface micrometer-scale discharges each confined in a hollow surface electrode, as detailed in previous reports [20, 27, 35] and in figures 2 and 3(a). This arrangement means that some physicochemical processes are negligible, for example Taylor cone and short-living ionic species [8] thus greatly simplifying the physical model of the interactions. It should be noted that SMD itself represents an important class of CAP for biomedical applications [20, 21, 33, 34] so this study has direct practical significance.

The paper is organized as follows: the experimental setup and the numerical model are described in sections 2 and 3, respectively. Section 4 discusses the simulation results for the gas and liquid regions supported with experimental data and with discussions on mass transfer, chemical conversion and biological effects. Concluding remarks are given in section 5. The aqueous chemistry data used in the model is provided in the appendix A.

2. Experimental setup

As shown in figure 2, the experimental setup consists of an SMD reactor and a downstream petri dish of deionized water, separated from each other by a nominal gas gap of $L_g = 0.01$ m. The depth of the deionized water is nominally $L_w = 0.01$ m, and the diameter of the circular petri dish is much smaller than the width of the surface plasma to allow for 1D treatment in numerical simulation. The SMD reactor consists of a plane HV electrode, a liquid-facing grounded mesh electrode, and a

dielectric sheet sandwiched between the two electrodes. Each grounded mesh has a hexagon shape with each of its size sides 4×10^{-3} m in length, 7.6×10^{-4} m in width and 5×10^{-4} m in thickness. Each mesh element supports a microdischarge, the details of which are reported previously [35, 36]. Gaseous reactive plasma species diffuse through the air gap and some of them penetrate into the deionized water.

As shown in figure 3(a), the plasma is stronger on the edge than in the center of each mesh but mesh-to-mesh homogeneity is good over the whole mesh-electrode surface. A sinusoidal high voltage of $V_{pp} = 11$ kV and $f = 10$ kHz were applied on the HV electrode with an averaged deposited power density of 500 W m^{-2}. The temperature of the mesh electrode measured with a thermocouple was found to remain roughly 300 K after 100 s of plasma treatment. Measured with a high-voltage probe (Tektronix, P6015A) and a current monitor (Tektronix, P6021), the applied voltage and the discharge current are shown in figure 3(b). In addition, the voltage–charge (V–Q) figure was measured (data not shown) by using a small capacitance of 0.1 μF, from which the discharge gap voltage (V_g) during gas breakdown was found to be around 1 kV. This indicates that each breakdown event occurs when the absolute value of the gas voltage reaches 1 kV approximately. V_g is illustrated as a red broken line in figure 3(b), of which the data is fitted for the time when the gas is not broken down. As will be discussed in section 3, the average absolute value of V_g, $|V_g|_{av}$, is useful in our model to quantify the power dissipation.

The densities of selected plasma species were measured both in the gas phase and liquid phase. In the gas phase, the O$_3$ density was measured by means of UV absorption spectroscopy as widely reported in literature [33, 39]. Here, we use a deuterium lamp (Ocean Optics, DH2000) to produce a line light across the downstream area of the plasma, parallel to and
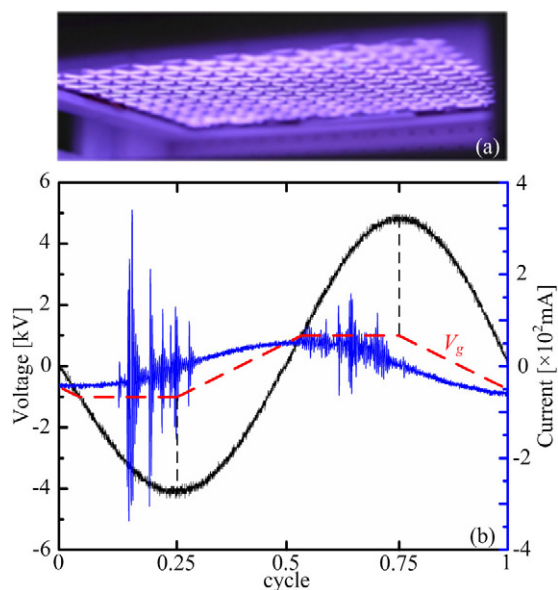
Figure 3. (a) An image of the SMD with (b) its applied voltage (black), the gas gap voltage (red) and current (blue).

at 5×10^{-3} m below the mesh electrode. The spectral line of $\lambda = 253.75$ nm was recorded by a spectrometer (Ocean Optics, Maya 2000 Pro). In the liquid phase, the density of O_{3aq} was measured using a spectrophotometry method, in which an indigo reagent (AccuVac® Ozone Reagent, Low Range 0 ~ 0.25 mg L^{-1}) was utilized and the absorption spectral at $\lambda = 600$ nm was recorded by a spectrophotometer (Hach, DR3900). A pH probe (Sartorius, PB-10) was used to measure the pH value of PAW, from which the number density of H^{+}_{aq} can be obtained. The concentrations of hydrogen peroxide (H_2O_{2aq}) and nitrate/nitrite were measured by using a microplate reader (Thermo Scientific Varioskan® Flash Reader). The Amplex® Red reagent was added into the water immediately after the SMD treatment, and it reacted with H_2O_{2aq} in a 1 : 1 stoichiometry to produce a red-fluorescent oxidation product, which was excited at $\lambda = 550$ nm and emitted at $\lambda = 595$ nm. Similarly, the Griess reagent was added into the water to detect nitrate/nitrite, and the absorbance was measured at $\lambda = 550$ nm. The measurements of H_2O_{2aq} and nitrate/nitrite were performed according to the manufacturer's protocol, similar to those reported in literature [20]. Moreover, the detection of free radicals like O^{-}_{2aq}, NO_{aq} and OH_{aq} in the PAW was based on an X-band ESR (Bruker BioSpin GmbH, EMX). For O^{-}_{2aq} and OH_{aq} concentration measurements, 5,5-dimethyl-1-pyrrolineN-oxide (DMPO) was used as a spin-trapping reagent. The spin adduct of DMPO•/OH_{aq} and DMPO•/OOH_{aq} generates a special feature with a peak intensity ratio of 1 : 2 : 2 : 1. Also, the DETC-Fe^{2+} complex was used to trap NO_{aq}, and the resulting stable product, (DETC)$_2$-Fe^{2+}-NO_{aq}, was detected by the electron spin resonance spectrometer. The ESR measurement was performed according to the manufacturer's protocol, similar to that in [36]. Concentration measurement for each plasma species was repeated three times.

ROS/RNS-containing reference media (e.g. H_2O_{2aq}) were used for instrument calibration. ESR calibration followed the manufacturer's standard procedure using non-plasma donors

of O^{-}_{2aq}, OH_{aq} and NO_{aq} and manufacturer-supplied calibration software. The accuracy of the pH probe, Sartorius PB-10, was within 0.005 and was confirmed with tests using pH buffers. The uncertainties associated with the instrument calibrations were much smaller than the difference between the experimental and simulation data reported here.

3. Description of the computational model

Our goal here is to develop an experimentally validated model for uncovering the chemical identity and the dose profile of main aqueous ROS/RNS reaching a sample lying deep inside the liquid. For indirect plasma-liquid interactions, it is beneficial and realistic to integrate a system-level simulation for the plasma region, the gas gap and the liquid bulk simultaneously. This is inspired by the technique and benefits of system science, and it enables a direct link of plasma dynamics to aqueous chemistry. Figure 4 shows the structure of the model and its computation flow-chart, with all three regions simulated together.

For the plasma generation region, it is noted that the SMD in air is typically filamentary and requires a 3D description particularly for dynamics and chemical kinetics within microdischarges. Here our interest is how gaseous plasma species pass through the air gap and reach the remote liquid surface. It has been shown that a liquid layer can filter out the impact of upstream short-living species [16], suggesting that it may be justified to simplify the treatment of the 3D dynamics of the streamers [33]. This is supported by the fact that the microdischarge patterns of our SMD remain the same from one mesh element to another and the gas transport away from the electrode is laminar. In fact, this approach has been employed for SMD in air with a global model for both the plasma generation and the gas diffusion regions without the presence of any liquid [33]. For the plasma generation region, our model uses a similar global model to [33]. However our model uses a 1D fluid model for the air gap and is therefore different from [33]. Fluxes of plasma species from the plasma generation region to the gas gap are used to integrate the two regions.

Our global model of the plasma generation region includes 53 species and 624 chemical reactions as listed in table 1, identical to those in [33] with the same set of reaction rates. In the air gap, a 1D fluid model employs the neutral species of this set of plasma species as no ionic species could survive more than 3 mm into the air gap (see discussion of table 3 and also in [33]). For the liquid layer, 109 chemical reactions among 33 species and their coefficients are listed in appendix A together with the references from which they are taken (see further discussion below). The reaction rates in table 1 and appendix A are from multiple sources in literature. How sensitively these reaction coefficients may affect simulation results is indirectly verified with good agreement between simulation predictions and experimental measurements of gas- and liquid-phase ROS/RNS. This will be discussed in figures 7, 12 and 14. This verification also applies to the transport coefficients in tables 2–4.
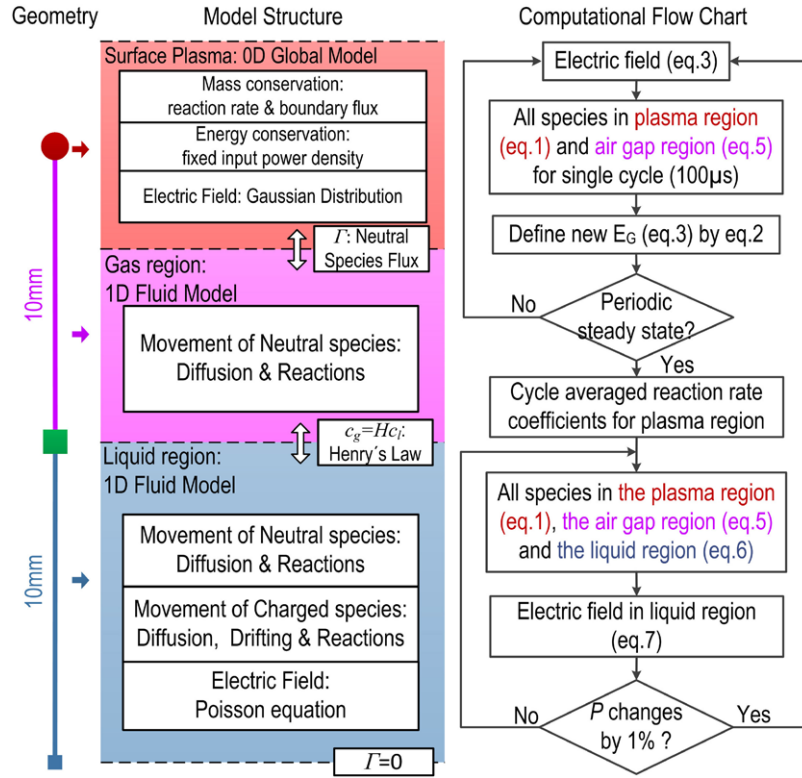
Figure 4. System-level model of plasma-liquid interactions, the model structure and the computational flow chart.

For mass transport in the plasma region, the governing equations consist of a mass conservation equation for each species, an energy conservation equation and an electric field equation. More specifically the mass conservation equations are

$$\frac{\partial n_{p,i}}{\partial t} = R_{p,i} - \frac{\Gamma_{pg,i}}{d_p} \quad (1)$$

where n_p is the number density of species in the plasma, R_p the reaction rate, Γ_{pg} the particle flux between the plasma region and the air gap region, and d_p the thickness of the plasma region. d_p is set to be 1×10^{-4} m, according to the typical radius of discharge filaments. The subscript i represents the ith species.

The energy conservation equation and electric field equation are given in equations (2) and (3), respectively

$$P = \frac{d_p}{T} \int_0^T \sum_i Z_i \mu_i n_{p,i} \left(E_G + \frac{|V_g|_{av}}{d_g} \right)^2 dt \quad (2)$$

$$E_G = E_m \exp\left(-\frac{1}{2} \left(\frac{t - 5\tau_{pls}}{\tau_{pls}} \right) \right) \quad (3)$$

where P represents the cycle-average power density, and T is the period of a discharge cycle. For our experiments, $P = 500$ Wm^{-2} and $T = 100$ μs. Z is the absolute value of the charge and μ is the mobility. The electric field is not calculated by Poisson's equation, but instead uses an experimentally derived field, E_G, having a Gaussian-like pulsed profile as given in equation (3), similar to the technique used in [33]. E_G has a maximum value of E_m and a pulse width of $\tau_{pls} = 1$ ns (the

duration of a single filament). E_m is a dependent variable that needs to be calculated based on equations (2) and (3). The time-averaged absolute value of V_g, $|V_g|_{av}$, is obtained from the voltage–charge figure. d_g represents the length of the discharge filaments, and it is assumed to be 3×10^{-3} m, i.e. the apothem of each mesh. Similar to previous global models for atmospheric plasma [13, 33], a relationship between the electron temperature and the electric field is obtained from solving the electron Boltzmann equation using Bolsig +. With this, equation (1) is solved to obtain the particle densities including electron density.

The electric field equation of (3) is modified from Sakiyama's work [33] with an additional term of $|V_g|_{av}/d_g$. The actual electric field used in our model is $E = E_G + |V_g|_{av}/d_g$. E_G calculated from equation (3) is very high during a current pulse, corresponding to the duration of a single breakdown. However, it is reduced to very small values beyond that. This is not always accurate for the actual electric field because the discharge gap voltage V_g remains high for a much long time in each half-cycle as shown in figure 3. The lifetimes of charged species are normally longer than the duration of a filament, and as such residual charged species are continuously accelerated by the electric field, which is estimated as $|V_g|_{av}/d_g$ in equation (2). Considering that $|V_g|_{av}/d_g$ consumes much input power used mainly for the acceleration of ionic species and that the density decay time for ions is about 300 ns, much longer than that for electrons (<3 ns) [33], this modification is likely to lower the density of plasma species several times. This modification is found to lead to a much closer agreement between the numerical and experimental results, as will be discussed in figure 7.

Table 1. Species considered in the model.

Plasma region	Cations	N^+, N_2^+, N_3^+, N_4^+, NO^+, N_2O^+, NO_2^+, H^+, H_2^+, H_3^+, O^+, O_2^+, O_4^+, OH^+, H_2O^+, H_3O^+
	Anions	e, O^-, O_2^-, O_3^-, O_4^-, NO^-, NO_3^-, H^-, OH^-, N_2O^-, NO_2^-
	Neutrals	$N(^2D)$, $N_2(A^3\Sigma)$, $N_2(B^3\Pi)$, H, N, H_2, N_2, H_2O, $O(^1D)$, O, $O_2(a^1\Delta)$, O_3, OH, HO_2, H_2O_2, O_2, NO, NO_2, NO_3, N_2O_3, N_2O_4, N_2O_5, HNO_2, HNO_3, N_2O, HNO
Air gap region		NO, N_2O, NO_2, NO_3, N_2O_3, N_2O_4, N_2O_5, HNO, HNO_2, HNO_3, N, N_2, O_2, O, $O_2(a^1\Delta)$, O_3, OH, HO_2, H_2O_2, H_2, H_2O
Liquid region		O_{aq}, $O_2(a^1\Delta)_{aq}$, O_{3aq}, OH_{aq}, HO_{2aq}, HO_{3aq}, H_2O_{2aq}, N_{2aq}, O_{2aq}, H_{aq}, H_{2aq}, N_2O_{3aq}, NO_{aq}, NO_{2aq}, NO_{3aq}, N_2O_{4aq}, N_2O_{5aq}, HNO_{2aq}, H^+_{aq}, $HO_2^-{}_{aq}$, $OH^-{}_{aq}$, $O^-{}_{aq}$, $O_2^-{}_{aq}$, $O_3^-{}_{aq}$, $NO_2^-{}_{aq}$, $NO_3^-{}_{aq}$, O_2NOOH_{aq}, $O_2NOO^-{}_{aq}$, $ONOO^-{}_{aq}$, $ONOOH_{aq}$, HNO_{3aq}, N_2O_{aq}, H_2O_{aq}

Table 2. Estimated diffusion distance of ionic species.

Species	EDL[m]	Species	EDL[m]
N^+	1.1×10^{-7}	OH^+	2.8×10^{-7}
N_2^+	2.2×10^{-7}	H_2O^+	3.1×10^{-7}
N_3^+	7.4×10^{-7}	H_3O^+	3.3×10^{-5}
N_4^+	7.0×10^{-8}	O^-	5.4×10^{-7}
NO^+	3.0×10^{-5}	O_2^-	1.4×10^{-6}
NO_2^+	7.1×10^{-5}	O_3^-	1.3×10^{-6}
N_2O^+	4.5×10^{-7}	O_4^-	2.0×10^{-6}
O^+	1.0×10^{-7}	NO^-	3.6×10^{-7}
O_2^+	2.1×10^{-6}	NO_2^-	9.4×10^{-6}
O_4^+	1.6×10^{-5}	NO_3^-	6.2×10^{-5}
H^+	2.0×10^{-7}	N_2O^-	6.7×10^{-5}
H_2^+	2.1×10^{-7}	H^-	2.7×10^{-7}
H_3^+	4.7×10^{-7}	OH^-	1.8×10^{-6}

Table 3. Henry's coefficients.

Species	H^{CC}(25 °C)	Ref.
N_2O	0.611	[43]
NO	0.046	[43]
NO_2	0.978	[44]
NO_3	44	[45]
N_2O_3	14.67	[46]
N_2O_4	36.67	[46]
N_2O_5	51.34	[47]
HNO_2	1198	[48]
HNO_3	5.1×10^6	[49]
O_3	0.2298	[50]
OH	733.5	[51]
H_2O_2	2.1×10^6	[52]
HO_2	1.39×10^5	[53]
H_2	0.191	[43]
O	3.2×10^{-2}	[41][a]
$O_2(a^1\Delta)$	3.2×10^{-2}	[41][a]

[a] Assumed the same as O_2.

The diffusion of gaseous plasma species through the air gap towards the downstream liquid sample is limited by their lifetimes. Diffusion distance can be estimated from the Einstein–Smulochowski equation [40]:

$$\text{EDL} = \sqrt{6D_g\tau} \qquad (4)$$

where EDL represents the effective diffusion distance, D_g is the diffusion coefficient in air and τ is the effective lifetime. The effective lifetimes of ionic species are obtained from their reaction rates in the plasma region. As listed in table 2, EDL varies in a range of 7×10^{-8} m for N_4^+ to 7.1×10^{-5} m for NO_2^+—thus no more than 1×10^{-3} m into the air gap. Therefore, only neutral species are considered for the air gap region in our model. As a result, a 1D diffusion model is developed for the air gap region, including 21 species (see table 1) and 63 chemical reactions. The governing equation is as follows:

$$\frac{\partial n_{g,i}}{\partial t} - D_{g,i}\nabla^2 n_{g,i} = R_{g,i} \qquad (5)$$

where n_g represents the number density of species in the air gap region, D_g the diffusion coefficient in air, and R_g the reaction rate.

Some of the gaseous species can go through the air gap and then penetrate into the liquid region. Henry's Law is used to describe the concentration balance of a given species between the gas phase and the liquid phase, and Henry's coefficients are listed in table 3. It is noted that the gas–liquid interface, an aerosol layer, has different features from those in both the gas and the liquid bulks. For example, it is predicted by molecular dynamic simulation that both hydrophobic species (e.g. O_{3aq}) and hydrophilic species (e.g. OH_{aq}, HO_{2aq} and H_2O_{2aq}) have a free-energy minimum at the interface, which means that the concentrations of such species are comparably higher in the interface layer than in the liquid volume [41, 42]. The unique features of the interfacial layer have an effect on the interaction processes between the SMD and the deionized water, for which there is a lack of relevant data of the interface layer. The thickness of such a layer is also very small, typically ~1 nm [41, 42], less than the physical scale of the plasma-liquid system by seven orders of magnitude, suggesting a local influence. The impact of this local influence on the downstream aqueous chemistry is likely to be heavily damped by rapid reactions in the dense liquid. Given these, it is reasonable to

J. Phys. D: Appl. Phys. 48 (2015) 495201

Z C Liu *et al*

Table 4. Diffusivity of aqueous species.

Species	Diffusivity [m² s⁻¹]	Ref.
O_{aq}	2×10^{-9}	[54]
$O_2(a^1\Delta)_{aq}$	2.0×10^{-9}	[54][a]
O_{3aq}	1.75×10^{-9}	[55]
OH_{aq}	2.0×10^{-9}	[56]
HO_{2aq}	1.0×10^{-9}	[b]
HO_{3aq}	1.0×10^{-9}	[b]
H_2O_{2aq}	1.0×10^{-9}	[57]
H_{2aq}	4.5×10^{-9}	[54]
H_{aq}	8.0×10^{-9}	[56]
H^+_{aq}	9.312×10^{-9}	[58]
OH^-_{aq}	5.26×10^{-9}	[58]
HO^-_{2aq}	1.0×10^{-9}	[b]
O^-_{aq}	2.0×10^{-9}	[c]
O^-_{2aq}	2.0×10^{-9}	[c]
O^-_{3aq}	1.75×10^{-9}	[c]
N_2O_{aq}	2.1×10^{-9}	[59]
NO^-_{3aq}	1.9×10^{-9}	[60]
NO^-_{2aq}	1.85×10^{-9}	[c]
HNO_{2aq}	1.85×10^{-9}	[61]
HNO_{3aq}	2.6×10^{-9}	[62]
O_2NOOH_{aq}	1.0×10^{-9}	[b]
$O_2NOO^-_{aq}$	1.0×10^{-9}	[b]
N_2O_{4aq}	1.0×10^{-9}	[b]
N_2O_{3aq}	1.0×10^{-9}	[b]
N_2O_{5aq}	1.0×10^{-9}	[b]
NO_{aq}	2.21×10^{-9}	[63]
$ONOOH_{aq}$	2.6×10^{-9}	[d]
$ONOO^-_{aq}$	1.9×10^{-9}	[e]
NO_{2aq}	1.85×10^{-9}	[61]
NO_{3aq}	1.0×10^{-9}	[64]

[a] Assumed the same as O_{2aq}.
[b] Assumed to be 1.0×10^{-9} m² s⁻¹.
[c] Assumed the same as their neutral species—for instance the diffusivity of O^-_{aq} is assumed the same as O_{aq}.
[d] Assumed the same as HNO_{3aq}.
[e] Assumed the same as NO^-_{3aq}.

neglect the nanoscale interfacial processes in our model as an approximation.

Finally the liquid region is treated with a 1D model, considering the drift motion, the diffusion motion and the aqueous chemistry. In the liquid phase, some species such as HNO_{3aq} are likely to hydrolyze into ionic species to set up an electric field. The movement of ionic species is then controlled by both the density gradient and the field. Therefore, the governing equations consist of the drift–diffusion equation for the mass conservation and Poisson's equation for the electric field, as follows:

$$\frac{\partial n_{l,i}}{\partial t} + \nabla \cdot (-D_{l,i} \nabla n_{l,i} + Z_i u_{l,i} n_{l,i} E) = R_{l,i} \quad (6)$$

$$\frac{\partial E}{\partial x} = \sum Z_i n_{l,i}/\varepsilon \quad (7)$$

where n_l is the number density of species in the liquid region, D_l the diffusion coefficient in water, μ_l the mobility of the charged species in water, R_l the aqueous reaction rate, and ε the dielectric constant. The diffusion coefficients of the aqueous molecules considered are listed in table 4, and the drift coefficients of charged species are obtained from the Einstein relation. The model has 33 species (see table 1) and 109 chemical reactions, including 21 reversible reactions (see appendix A).

It is worth stating that most of the reaction coefficients used in this study (those from [33] and in appendix A) are obtained from multiple sources in literature. Possible uncertainties in the experiments from which these reaction coefficients were obtained can in principle introduce errors to our simulation prediction, an inevitable and common risk to all numerical simulations of non-equilibrium atmospheric pressure gas discharges. To provide direct evidence of whether our simulation results are realistic, they are compared with experimental measurement with good agreement (see figures 7, 12(b) and 14).

A commercial software, COMSOL Multiphysics@, was used for constructing three sub-models, and these sub-models were used as one system-level master model and simulated simultaneously. In other words, a master hybrid model is formed with the integration of one 0D global model (for plasma generation) and two 1D fluid models (for the air gap and liquid regions). The hybrid model has a similar topological structure to the experimental setup, with only the plasma region simplified with a 0D description. The initial gas composition is 76.63% N_2, 20.37% O_2 and 3% H_2O by considering water evaporation [15]. The initial pH value is set to be 7, i.e. the densities of both H^+_{aq} and OH^-_{aq} are 6.02×10^{19} m⁻³. The dissolution of O_{2aq} and N_{2aq} in the water is considered to be in equilibrium with the air. The initial density of other species in the plasma, air gap and water is set to be 10^5 m⁻³. The plasma, the buffer air gap and the water layer are assumed to be at a constant room temperature of 300 K, consistent with experimental data. The boundary condition for the water bottom is set to be $\Gamma = 0$, assuming that no species is absorbed by the petri dish surface. In fact, no plasma-induced species can penetrate through the water bulk to the bottom of the petri dish in this study, as the plasma-on time is 100 s at most.

4. Results and discussion

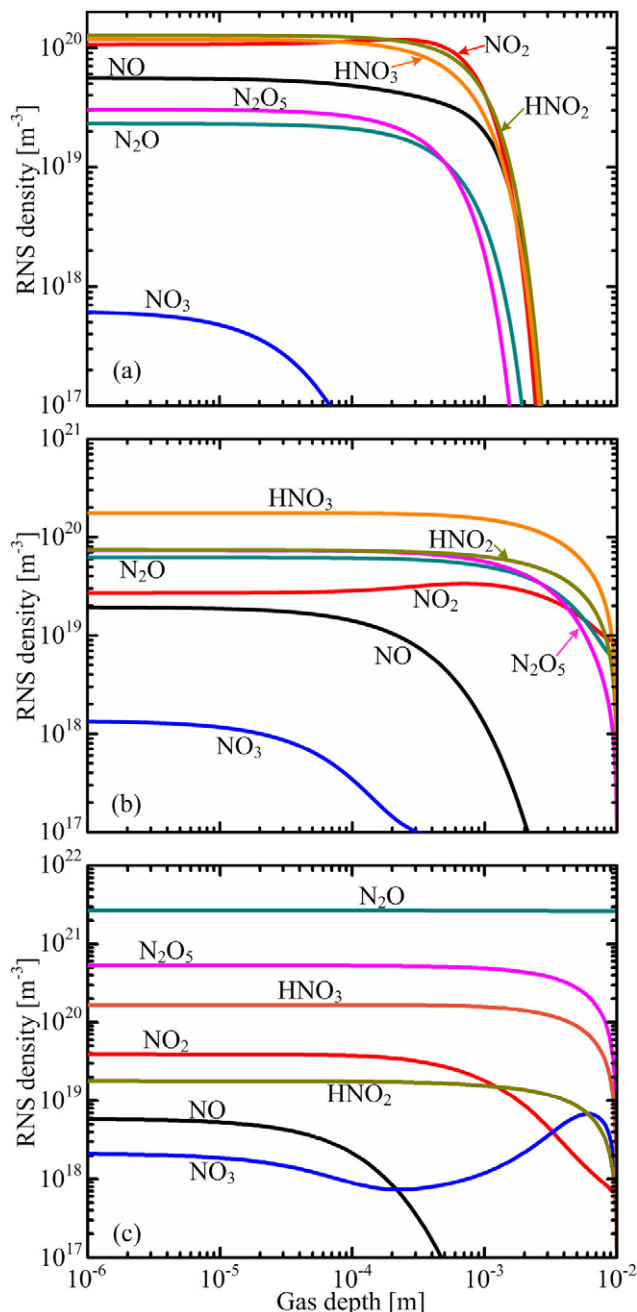### 4.1. Reactive species through the air gap region

Figures 5 and 6 show the diffusion patterns of neutral plasma species from the plasma region into the air gap region at a plasma-on time of 0.01 to 100 s. The threshold concentration of 10^{17} m⁻³ used in figures 5 and 6 is about 3.7 ppb (parts per billion). For reactive oxygen species (ROS), shown in figure 5, only O_3 and H_2O_2 can propagate through the air gap to reach the downstream sample at $L_g = 0.01$ m within one second of the plasma-on time. The third and fourth most penetrating ROS through the air gap are HO_2 and $O_2(a^1\Delta)$, and for a plasma-on time of 1–100 s their concentrations drop to 10^{17} m⁻³ after 4.5×10^{-3}–7×10^{-3} m and 1×10^{-3}–4.7×10^{-3} m into the air gap, respectively. For O and OH concentrations not to fall below 10^{17} m⁻³, their diffusion distance needs to be
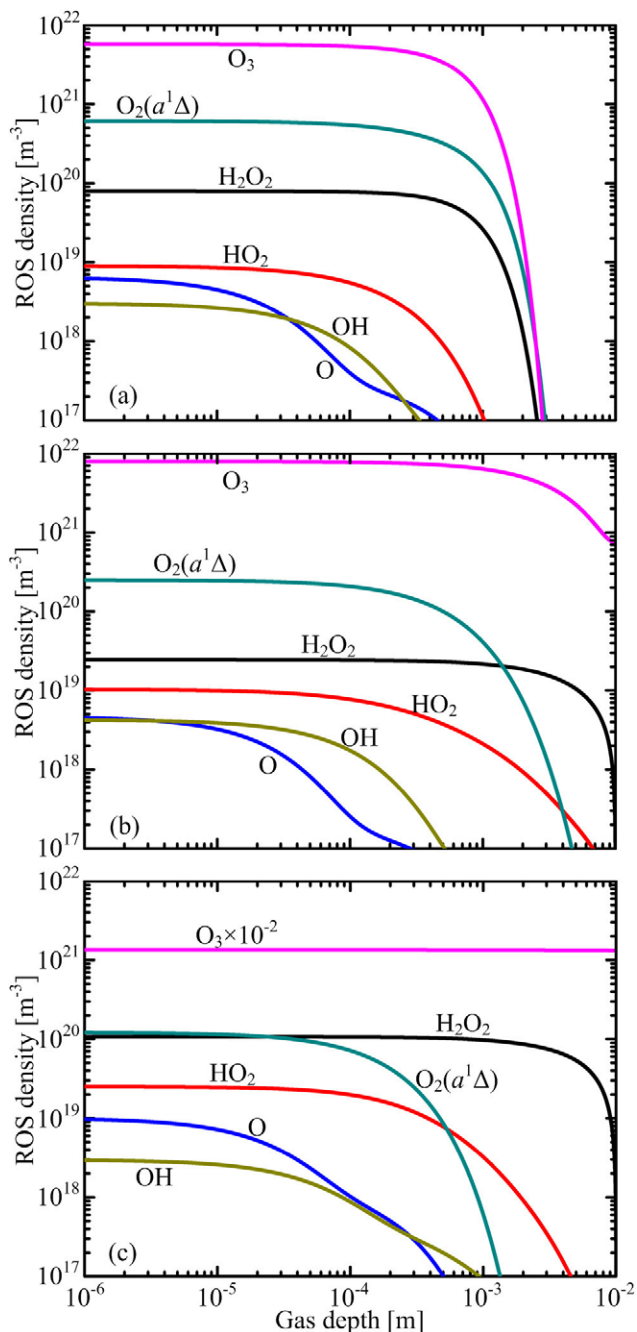
Figure 5. ROS diffusion into the air gap after a plasma-on time of (a) 0.01 s; (b) 1 s; and (c) 100 s.

Figure 6. RNS diffusion into the air gap after a plasma-on time of (a) 0.01 s; (b) 1 s; and (c) 100 s.

restricted to less than 1×10^{-3} m. It is worth noting that O, OH, $O_2(a^1\Delta)$ and HO_2 all have an EDL smaller than 1×10^{-3} m (see table 5). Near the surface of the downstream liquid at a plasma-on time of 0.01–100 s, the dominant gaseous ROS are O_3 and H_2O_2, which have decreasing concentrations except for O_3 at $t = 100$ s. The gas-phase O_3 density near the liquid surface reaches the same level as the value at the exit of the plasma-generation region before $t = 100$ s. This is largely because the small Henry's coefficient of O_3 restricts its dissolution in the ionized water and in turn increases its accumulation in the air gap. By contrast, the Henry's coefficient of H_2O_2 is sevenfold greater than that of O_3 (see table 3) and this leads to a marked reduction of gas-phase H_2O_2 near the liquid surface.

Compared with ROS, reactive nitrogen species (RNS) capable of reaching the liquid surface are more numerous. Figure 6 suggests that NO_2, HNO_2, HNO_3, N_2O_5 and N_2O are capable of reaching the gas-liquid interface with a gaseous concentration above 10^{17} m^{-3} before $t = 1$ s. After $t = 1$ s but before $t = 100$ s, NO_3 also reaches the liquid surface and its concentration hike beyond 1×10^{-3} m into the liquid bulk is due to chemical reactions in the air gap. However, the biologically significant NO has a short diffusion distance of EDL $< 1 \times 10^{-3}$ m (see table 5). At $t = 0.01$ s, its concentration drops to 10^{17} m^{-3} around 4.4×10^{-3} m into the gas gap and its diffusion reach reduces progressively with increasing time suggesting strong loss mechanisms through plasma chemistry in the air gap. Together with the fact that Henry's

J. Phys. D: Appl. Phys. **48** (2015) 495201

Z C Liu *et al*

Table 5. Diffusion distance into the air gap at $t = 100$ s.

| Species	Over 10^{17} m^{-3} (m)	EDL (m)
H_2O_2	>0.01	>0.01
HO_2	4.6×10^{-3}	3.7×10^{-4}
OH	8.7×10^{-4}	1.3×10^{-4}
O	4.4×10^{-4}	6×10^{-5}
O_3	>0.01	>0.01
$O_2(a^1\Delta)$	1.2×10^{-3}	4.6×10^{-4}
HNO_3	>0.01	>0.01
HNO_2	>0.01	>0.01
NO	4.4×10^{-4}	2.0×10^{-4}
NO_2	>0.01	>0.01
N_2O_5	>0.01	>0.01
NO_3	>0.01	>0.01

Figure 7. Numerically and experimentally obtained O_3 concentration at 5×10^{-3} m below the plasma exit. Sakiyama's data are from [33].

coefficient of NO is very small (table 3), this suggests that it is ineffective to use air plasma as a source for aqueous NO.

Of RNS that can reach the liquid surface, the dominant RNS in terms of concentration changes identity with time—it is HNO_2 at 0.01 s, HNO_3 at 1 s and N_2O at 100 s, hinting the strong influences of mutual chemical reactions and dissolution. For N_2O, its concentration at the exit of the plasma region increases modestly from 2.3–6.2×10^{19} m^{-3} when the plasma-on time increases from $t = 0.01$ s to 1.0 s. This increase is likely to be due to the plasma chemistry in the air gap. However its dissolution into the deionized water is very limited as seen in its small Henry's coefficient of 0.611 (table 3). As a result, the N_2O concentration jumps to about 2.7×10^{21} m^{-3} at $t = 100$. This is similar to the case of O_3 in figure 5. For HNO_2, its concentration at the plasma exit is seen in figure 5 to decrease from 1.25×10^{20} m^{-3} at $t = 0.01$ s to 7.5×10^{19} m^{-3} at $t = 1$ s and 1.8×10^{19} m^{-3} at $t = 100$ s. This decrease in HNO_2 before its arrival at the liquid surface is suggestive of the dominant influence of plasma chemistry in the air gap, whereas its loss to the liquid should also be important given its large Henry's coefficient of 1198 (see table 3). Similarly, the plasma chemistry in the air gap is likely to be responsible for the 1.5-fold increase of the HNO_3 concentration from $t = 0.01$ s to 1.0 s. The subsequent reduction in its concentration at $t = 100$ s is clearly due to the dissolution into liquid, given that the Henry's coefficient of HNO_3 is more than three orders of magnitude above that of HNO_2. It is therefore evident that the diffusion of plasma species through the buffering region of the air gap to the liquid is controlled by the plasma chemistry in the air gap and the dissolution into the liquid in a species-dependent fashion. Whilst understandable based on figures 5 and 6 but not widely appreciated, species with low concentrations in the air gap may have large aqueous concentrations (with exceptions such as NO) and as a result gas-phase ROS/RNS concentrations cannot be used to reliably predict their aqueous concentrations.

Detailed analysis of the generation and loss pathways to support the above conclusion is possible. For instance, $NO + OH + M \rightarrow HNO_2 + M$ is a main pathway for HNO_2 generation in the plasma region and its rate decreases because of the decreasing NO concentration from $t = 0.01$ s to
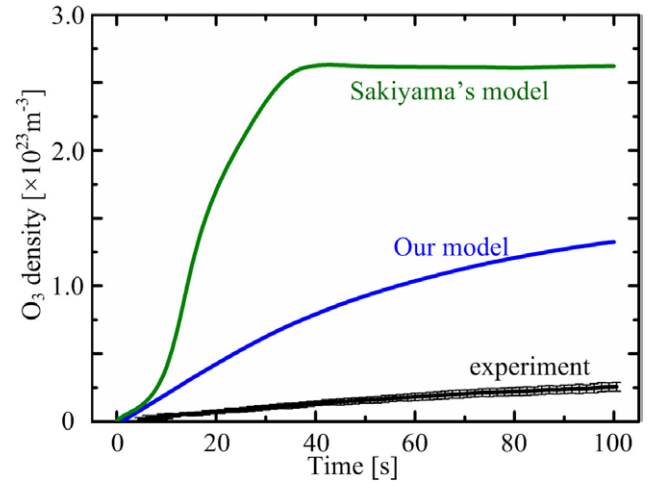
$t = 100$ s. In contrast to most species, NO_2 and NO_3 have their densities peaked in the vicinity of the water surface (at $t = 1$ s or $t = 100$ s, respectively). This is attributed to both their small Henry's coefficients and the reactions in the air gap region as follows:

$$NO_3 + HO_2 \rightarrow NO_2 + OH + O_2 \qquad (8)$$

$$O_3 + NO_2 \rightarrow NO_3 + O_2 \qquad (9)$$

$$N_2O_5 + M \leftrightarrow NO_2 + NO_3 + M \qquad (10)$$
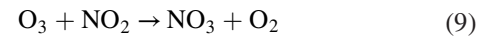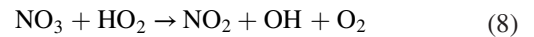
In order to validate the numerical model, the O_3 concentration at 5×10^{-3} m downstream from the liquid-facing electrode of the SMD was measured and the results are shown in figure 6. Numerically computed O_3 is seen to be about fivefold higher than the experimentally measured value, but with both following a very similar trend with time. As a reference point, the results of Sakiyama's model [33] were reproduced for O_3 and are included in figure 7. Their O_3 concentration is seen to be higher than our data by about twofold and its time dependence is also different with the O_3 concentration reaching a plateau after 40 s of plasma treatment. The difference is due to the consideration in our model of the electric field for ion acceleration after a breakdown (see discussion of equation (3)), which helps bring the simulation data closer to the experimental results. Our numerically calculated O_3 concentration is still about fivefold above the experimental value. Qualitatively this is understandable since our 1D model does not account for the radial escape of O_3 (either to the surrounding atmosphere in an open system or to the wall in a closed system).

From an application standpoint, the quantification of the gas-phase diffusion distances of reactive species is useful for an overview of their relative importance for a downstream sample. Using 10^{17} m^{-3} (or 3.7 ppb) as a threshold concentration (see table 5), biologically significant free radicals such as NO, OH, $O_2(a^1\Delta)$ and HO_2 and O have very short diffusion distances when their densities drop to the threshold concentration within 4.55×10^{-3} m into the air gap. The EDLs of
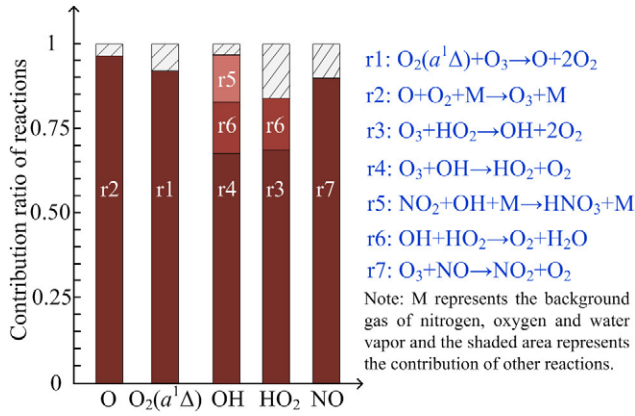
Figure 8. The main reactions for the loss of free radicals.

ROS in air plasma are even less than that in He + O$_2$ plasma mainly due to their diffusion coefficients being lower in air [65, 66]. These observations support the view from figures 4 and 5 (and [16]) that long-living species such as H$_2$O$_2$, O$_3$, HNO$_3$, and HNO$_2$ are dominant for indirect plasma treatment. Notwithstanding the discussion of aqueous ROS/RNS, indirect plasma has lower plasma dose than and different plasma chemistry to direct plasma, in which free radicals are likely to play an important role as seen in the case of bacterial inactivation [67, 68].

For free radicals such as O, NO, OH, O$_2$($a^1\Delta$) and HO$_2$, their generation in the air gap predominantly originates from their diffusion from the plasma region. Their losses are caused by chemical reactions to form more stable species such as O$_2$, H$_2$O$_2$, O$_3$ and HNO$_3$, as shown in figure 8. For example, O$_3$ plays a dominant role in the reduction of NO and O$_2$($a^1\Delta$), so the peak concentrations and diffusion distances of NO and O$_2$($a^1\Delta$) decrease with increasing O$_3$ concentration from $t = 1$ s to 100 s(see figures 5 and 6). In addition, O$_3$ is an important reactant for the loss of OH and HO$_2$. Besides the diffusion from the plasma region, the reaction of O + O$_2$ + M $\rightarrow$ O$_3$ + M also plays an important role for the production of O$_3$ in the air gap region.

4.2. Reactive species into the liquid region

The gaseous species dissolve into the deionized water and then further diffuse downwards. The diffusivity is lower than that in the gas phase by approximately four orders of magnitude (see table 4), and the chemistry is more intensive due to the much more frequent collisions between the reactive species and the water molecules.
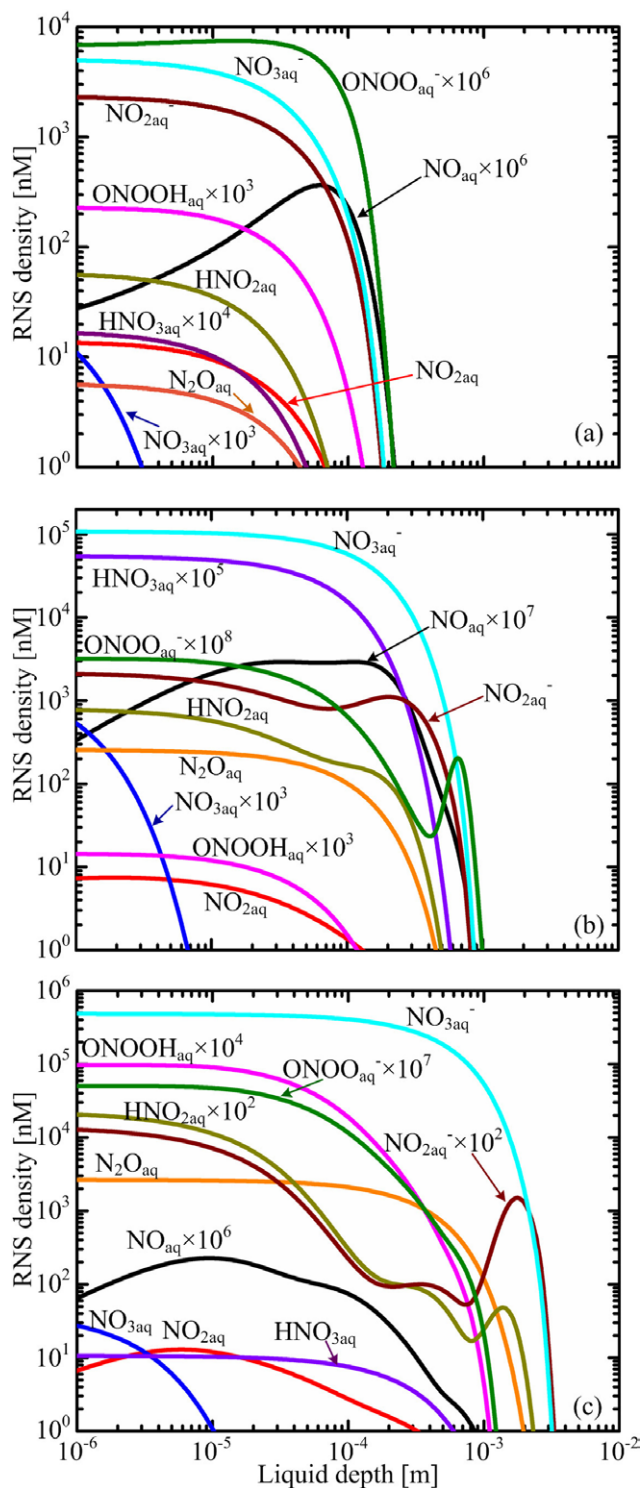
Figure 9 shows that the main aqueous ROS (with density higher than 1 nM, i.e. 6.023×10^{17} m^{-3}) are O$_{3aq}$, H$_2$O$_{2aq}$ and OH$_{aq}^-$, of which OH$_{aq}^-$ is generated by the self-ionization of water molecules. The initial value of OH$_{aq}^-$ density in the model is set to be 100 nM, corresponding to a pH value of 7. With the penetration of reactive plasma species, OH$_{aq}^-$ rapidly converts to other anions (mainly NO$_{2aq}^-$ and NO$_{3aq}^-$ as shown in figure 10) so its density falling-off point can serve as the indicator for the penetration depth of the incoming plasma species. Using this indicator, the penetration speed initially varies with time within the first few seconds and then
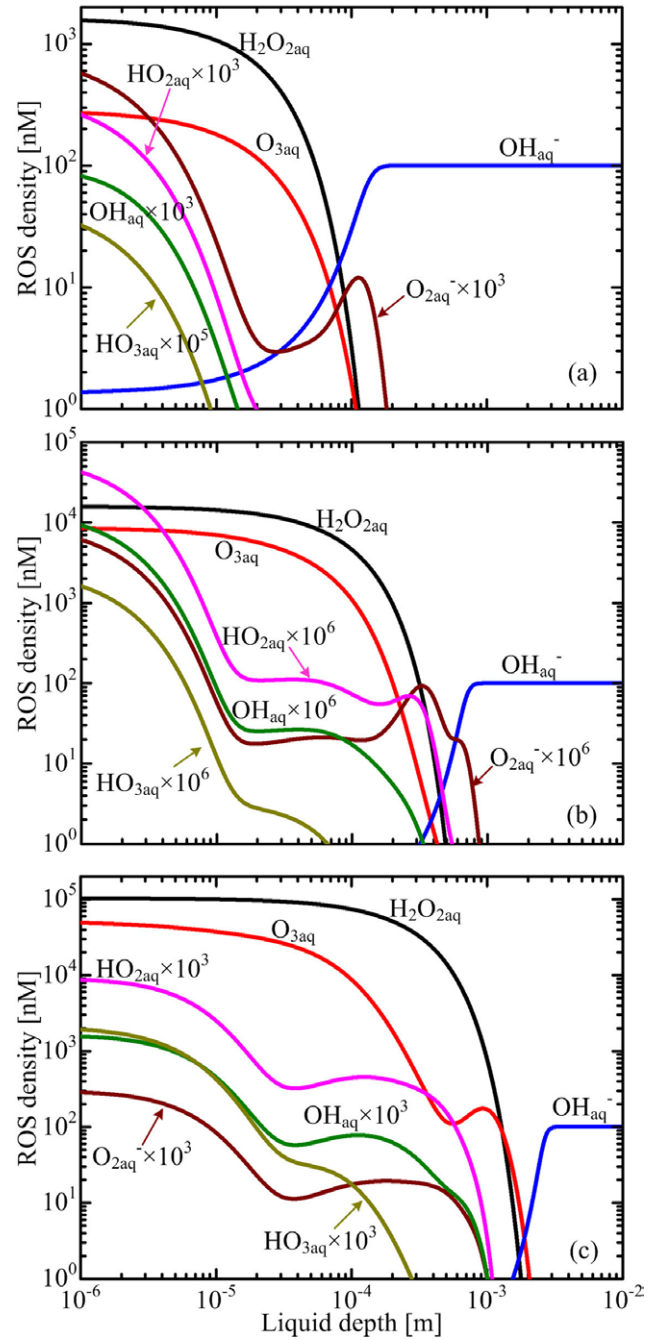
Figure 9. ROS penetration into the deionized water after a plasma-on time of (a) 1 s; (b) 10 s; and (c) 100 s.
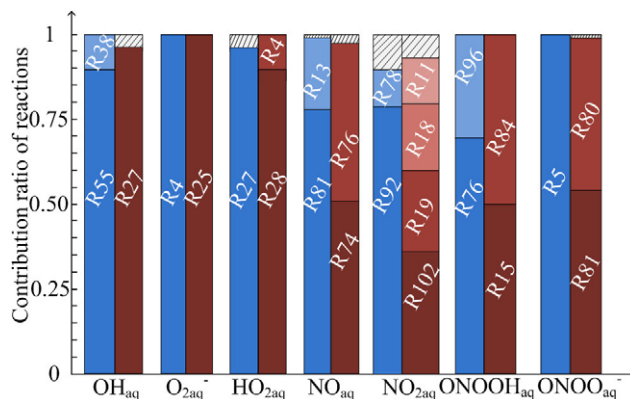
becomes constant at about 2.2×10^{-5} m s^{-1} after $t = 10$ s. It is evident from figure 9 that the H$_2$O$_{2aq}$ and O$_{3aq}$ concentrations follow very similar spatial profiles, both reaching their peak values at the gas–liquid surface and then following a very similar parabolic decay into the liquid bulk. This suggests that these two species have high chemical stability in the liquid phase and their distributions are diffusion-limited. The concentration of H$_2$O$_{2aq}$ is always threefold to fivefold higher than that of O$_{3aq}$, and this concentration ratio is similar to the experimental results reported by Shibata et al [21]. At $t = 100$ s, H$_2$O$_{2aq}$ and O$_{3aq}$ can reach around 2×10^{-3} m.

It should be noted that OH$_{aq}$, HO$_{2aq}$ and O$_{2aq}^-$ are regenerated in situ in the liquid phase even though little of their

Figure 10. RNS penetration into the deionized water after a plasma-on time of (a) 1 s; (b) 10 s; and (c) 100 s.

Figure 11. Main reactions for the generation (left bar in blue) and loss (right bar in dark red) of aqueous free radicals.

several μM [15, 16, 24, 69]. So the concentrations of OH_{aq}, O_{2aq}^- and HO_{2aq} in SMD are three orders of magnitude lower. The sub-nM concentrations of O_{2aq}^- and OH_{aq} in figure 9 suggest their limited direct role in biological effects; however, their *in situ* generation can be significant.

Figure 10 shows the spatial profile of RNS into the liquid bulk, from which it is evident that the dominant species is NO_{3aq}^-. For plasma treatment times no more than 10 s, the first four most abundant species of NO_{3aq}^-, NO_{2aq}^-, HNO_{2aq} and N_2O_{aq} can reach no more than 0.4×10^{-3}–0.8×10^{-3} m in the deionized water if their concentrations are maintained at or above 1 nM. With longer treatment times up to 100 s, their penetration depth improves to 2×10^{-3}–3×10^{-3} m. The descending oder of the aqueous RNS concentrations now changes to NO_{3aq}^-, N_2O_{aq}, HNO_{2aq} and NO_{2aq}^-, because more and more NO_{2aq}^- are oxidized to NO_{3aq}^- by O_{3aq} (R32, appendix A) (see figure 9). This also leads to local concentration maxima for HNO_{2aq}/N_2O_{aq} at the front part of the penetration. It is worth noting that NO_{aq}, a biologically significant molecule, is generated in very low concentrations of sub-nM in liquid by the surface plasma. RNS other than NO_{3aq}^-, NO_{2aq}^- and N_2O_{aq} can barely reach more than 2.3×10^{-4} m without their concentrations falling below 1 nM. Therefore NO_{3aq}^-, NO_{2aq}^-, and HNO_{2aq} are likely to be the most significant charged and neutral RNS with similar liquid penetration depths (of 2×10^{-3} –3×10^{-3} m at $t = 100$ s) to those of the most significant ROS of H_2O_{2aq} and O_{3aq}.

Hydrolysis of neutral gaseous species produces ionic species in liquid. While only neutral species diffuse through the air gap in figure 2, some hydrolyze to form ionic species in the water, such as H_{aq}^+, NO_{2aq}^- and NO_{3aq}^- [99, 100, 104]. The hydrolysis ratio decreases sharply with the plasma treatment due to the decrease of pH value (see figure 11). Take HNO_{2aq} for instance: the density ratio of $[NO_{2aq}^-]/[HNO_{2aq}]$ decreases from 77 at $t = 1$ s to 3.7 at $t = 100$ s.

Similar to the case of ROS, some short-living RNS are regenerated *in situ* such as NO_{aq} and peroxynitrite ($ONOOH_{aq}/ONOO_{aq}^-$). The peak density of NO_{aq} is below 1 nM, lower than the detection limit of ESR. As the isomer of HNO_{3aq}, $ONOOH_{aq}$ also hydrolyzes to H_{aq}^+ and NO_{3aq}^- mainly via its immediate state ($ONOOH_{aq}^*$) [70], or alternatively it

gaseous counterparts could survive passage through the air gap to reach the liquid. The spatial distribution profiles of these short-lived aqueous species are reaction-limited rather than diffusion-limited, and are much different from those of O_{3aq} and H_2O_{2aq}. The peak density of O_{2aq}^- and OH_{aq} is below 1 nM, lower than the detection limit of ESR. This is distinctly different from data of direct plasma-liquid interactions for which the concentrations of OH_{aq}, O_{2aq}^- and HO_{2aq} are in the range of

J. Phys. D: Appl. Phys. **48** (2015) 495201

Z C Liu *et al*

partially decomposes to NO_{2aq} and OH_{aq} [71]. Kushner *et al* reported an $[ONOO^-_{aq}]/[NO^-_{3aq}]$ ratio of ~0.5 in water directly treated by plasma [15]. This is higher than our data by six orders of magnitude, and is mostly likely due to the difference between direct and indirect plasma-liquid interactions. In the work of Kushner *et al*, the production ratio of ONOOH/ HNO_3 in the gas phase is about 40% and other short living species such as NO, OH, and HO_2 can transfer into the liquid phase. Therefore, $ONOOH_{aq}$ is generated in direct plasma-liquid interactions from either the gas–liquid diffusion or the liquid-phase reactions among short-living species. The latter include $NO_{2aq} + OH_{aq} \rightarrow ONOOH_{aq}$ (R15, appendix A) and $NO_{aq} + HO_{2aq} \rightarrow ONOOH_{aq}$ (R76, appendix A). However, in indirect plasma-liquid interactions as reported here, no gaseous short-living species can reach the liquid sample (see table 5) leading to a much lower $[ONOO^-_{aq}]/[NO^-_{3aq}]$ ratio. It is noted the gaseous ONOOH is neglected in our model, because its existence in ambient pressure and temperature has been questioned [69, 70], and even if it exists, in our case it is very unlikely to pass through the air gap due to its short lifetime of several milliseconds. Despite the much lower $[ONOO^-_{aq}]/[NO^-_{3aq}]$, the peak density of peroxynitrite is found to be around 9.7 nM at $t = 100$ s, not much lower than that of direct plasma-liquid interactions [15].

The main chemical reactions for aqueous free radicals are shown in figure 11. OH_{aq} is mainly generated by R38 (see appendix A): $O^-_{3aq} + H^+_{aq} \rightarrow O_{2aq} + OH_{aq}$ and R55: $HO_{3aq} \rightarrow O_{2aq} + OH_{aq}$, and reduced by R27 : $O_{3aq} + OH_{aq} \rightarrow HO_{2aq} + O_{2aq}$. A molecular dynamics study suggests that OH_{aq} has a long lifetime in pure water [72], but in our case the density of O_{3aq} is high thus preventing a large OH_{aq} concentration to be supported. O^-_{2aq} is mainly generated by the hydrolysis of HO_{2aq} (R4) and reduced also by the reaction with O_{3aq} (R25): $O_{3aq} + O^-_{2aq} \rightarrow O^-_{3aq} + O_{2aq}$. The hydrolysis of HO_{2aq} has been predicted to be the main pathway for its reduction in pure water by molecular dynamic simulation [73]; however in our case the reaction with O_{3aq} dominates (R28): $O_{3aq} + HO_{2aq} \rightarrow O_{2aq} + HO_{3aq}$. Also, O_{3aq} is the precursor for HO_{2aq} production via R27: $O_{3aq} + OH_{aq} \rightarrow HO_{2aq} + O_{2aq}$. Therefore as a whole, a chemical chain of $OH_{aq} \rightarrow HO_{2aq} \rightarrow HO_{3aq}$ exists via the reactions with O_{3aq}.

For RNS, NO_{aq} is mainly generated by R13: $2HNO_{2aq} \rightarrow NO_{aq} + NO_{2aq} + H_2O_{aq}$ and R81: $OH_{aq} + ONOO^-_{aq} \rightarrow O_{2aq} + OH^-_{aq} + NO_{aq}$. Its loss is via R74: $NO_{aq} + OH_{aq} \rightarrow NO^-_{2aq} + H^+_{aq}$ and R76: $NO_{aq} + HO_{2aq} \rightarrow ONOOH_{aq}$ as shown in figure 11. NO_{2aq} is mainly generated by R78: $OH_{aq} + HNO_{2aq} \rightarrow H_2O_{aq} + NO_{2aq}$ and R92: $NO_{3aq} + NO^-_{2aq} \rightarrow NO^-_{3aq} + NO_{2aq}$, and lost via R11: $2NO_{2aq} \leftrightarrow N_2O_{4aq}$, R18: $NO_{2aq} + HO_{2aq} \leftrightarrow O_2NOOH_{aq}$, R19: $2NO_{2aq} (+H_2O_{aq}) \leftrightarrow NO^-_{2aq} + NO^-_{3aq} + 2H^+_{aq}$ and R102: $NO_{2aq} + NO_{3aq} \rightarrow N_2O_{5aq}$. Besides $NO_{aq} + HO_{2aq} \rightarrow ONOOH_{aq}$ (R76) as the main reaction for $ONOOH_{aq}$ generation in direct plasma-liquid interactions [15], $HNO_{2aq} + H_2O_{2aq} \rightarrow ONOOH_{aq} + H_2O_{aq}$ (R96) plays an important role. On the other hand, $ONOOH_{aq} \rightarrow NO_{2aq} + OH_{aq}$ (R15) and $ONOOH_{aq} \rightarrow H^+_{aq} + NO^-_{3aq}$ (R84) are responsible for the majority of its loss. The two pathways for $ONOOH_{aq}$
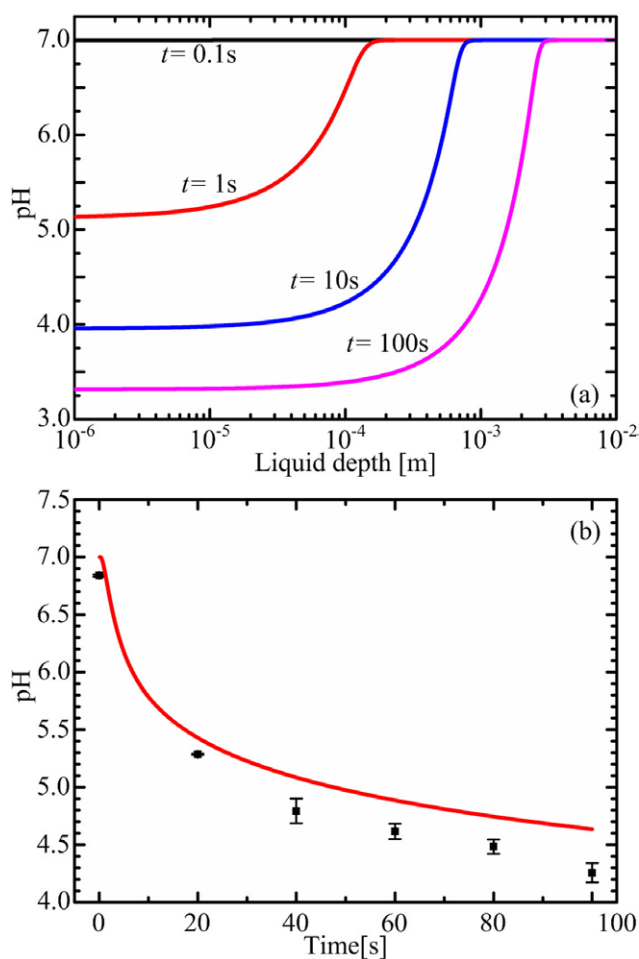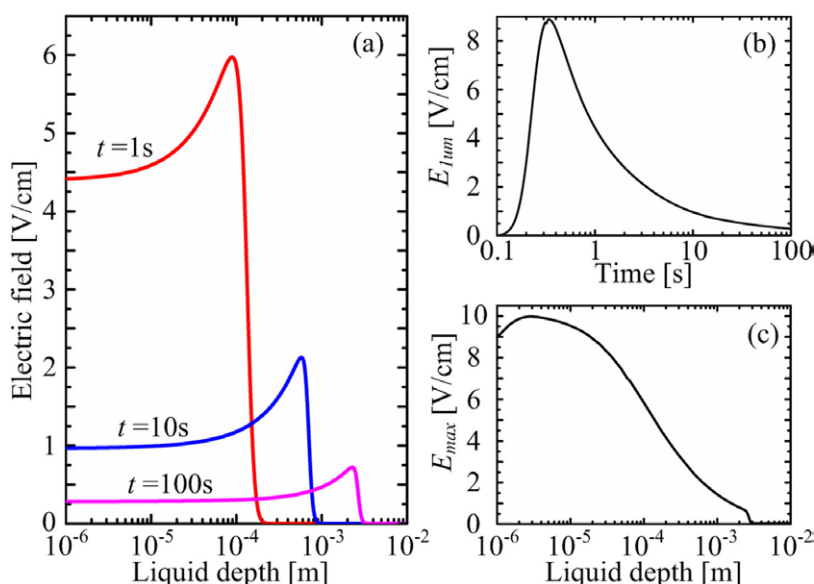
Figure 12. (a) Spatial distribution and (b) spatially averaged value of pH as a function of the plasma-on time.

loss are in agreement with [70, 71]. Finally, $ONOO^-_{aq}$ is generated by the hydrolysis of $ONOOH_{aq}$ (R5), while it is reduced by the reactions with OH_{aq} (R80 and R81).

4.3. Biological effects of plasma-activated water

With the main aqueous ROS and RNS established, we discuss here their possible effects on biological matter with the support of observations reported in literature and also from our own measurements. Of the main aqueous RNS, nitrate (HNO_{3aq}/NO^-_{3aq}) and nitrite (HNO_{2aq}/NO^-_{2aq}) are abundant with a total concentration of a few hundred μM. With their penetration into the liquid bulk, the pH value of the plasma-treated deionized water decreases due to the hydrolysis of these two species (to form nitric and nitrous acids). As a result, an electric field is formed due to the differences in movement velocities among the self-ionized species.

The dependence of the calculated pH value and electric field on the plasma treatment time is illustrated in figures 12 and 13, respectively. As shown in figure 12(a), the pH value at the gas–liquid interface keeps decreasing. At $t \sim 1.9$ s, the pH value at the liquid surface is found to decrease to 4.7, and this pH value is sometimes considered as an antimicrobial threshold since the microbial deactivation effect of PAW was found to increase sharply when pH < 4.7 [74]. As the pH

Figure 13. (a) spatial distribution of the electric field in the SMD-treated water; (b) the electric field at 1 μm as a function of time; (c) the peak electric field as a function of the water depth.

itself has little effect on microorganisms even for hydrochloric or nitric acid solutions with pH $=$ 3 [22], the biological effect should be due to the synergistic effect of the reactive plasma species and low pH value (pH $<$ 4.7) [75]. Different mechanisms have been put forward for this synergistic effect. One proposal is the hydrolysis of HO_{2aq} via $HO_{2aq} \leftrightarrow H_{aq}^+ + O_{2aq}^-$ (R4) because the pK_a value of HO_{2aq} is 4.8 [74]. In acidic solution of a pH $<$ pK_a value of HO_{2aq}, O_{2aq}^- is converted into HO_{2aq}. The latter can penetrate the cell membrane and then react with intracellular components [76]. On the other hand, the synergy effect could be due to $HNO_{2aq} + H_2O_{2aq} \rightarrow ONOOH_{aq} + H_2O_{aq}$ (R96) because the density ratio of $[HNO_{2aq}]/[NO_{2aq}^-]$ is higher as the pH value decreases thus benefiting the production of $ONOOH_{aq}$ [75]. The latter has high permeability and is thus extremely effective in eliciting damage to bacteria [76]. Although the biological effect of SMD-activated water was found to be significantly pH-dependent [70], both of the mechanisms need further examination because the volume-averaged concentrations of HO_{2aq} and $ONOOH_{aq}$ are lower than 1 nM (see figures 9 and 10).

The dependence of the spatial-averaged pH value on the SMD treatment time was measured and shown with numerically calculated data in figure 12(b). In general, the numerical and experimental results follow very similar trends with the numerical value higher by ~0.3 when $t >$ 40 s. According to the numerical results, the average pH value at $t =$ 100 s is 4.7, but in the surface layer of PAW the minimal pH value decreases to 4.7 just when $t \sim$ 1.9 s, and it is even down to 3.32 at $t =$ 100 s (see figure 12(a)). The much lower pH value in a thin surface layer of SMD-activated water is consistent with experimental observations obtained with a color forming method [30]. As shown in figure 12(a), the surface layer expands with a velocity of 2.2 $\times$ 10^{-5} m s^{-1}, the same as the penetration speed of reactive species. According to the expansion velocity, one can control the SMD treatment time for localized deactivation; for example, the effect of 100 repeated

treatments of 1 s each must be much more localized compared to one single treatment of 100 s. It should be emphasized here that the culture media used for both bacterial and mammalian cells have an inherent buffering capability and as such the pH values in figure 12 are likely to recover to or towards its physiological level.

As shown in figure 13(a), the absolute value of the electric field peaks near the water surface and the peak electric field shifts into the depth of the liquid with increasing time. We choose the location of a water depth of 1 μm to examine the time variation of the field, $E_{1\mathrm{um}}$. As shown in figure 13(b), $E_{1\mathrm{um}}$ increases quickly after the plasma species come in contact with the water at $t =$ 0.12 s, and it peaks at $t =$ 0.34 s and exhibits a 890 V m^{-1} magnitude after which it decreases hyperbolically. Figure 13(c) shows the maximum electric field as a function of the water depth and it reaches its maximum of 1 kV m^{-1} at a water depth of 2.85 $\times$ 10^{-6} m. Beyond 1.5 $\times$ 10^{-3} m, its value decreases to below 100 V m^{-1}. The peak value of the electric field is two to three orders of magnitude below what is required for cell electroporation or lysing, but may have an effect on cell gating [78]. The electric field felt by a bacterium 1 μm in size and suspended in the water is pulsed with a width of more than one second (see figure 13(b)). This duration is more than enough to establish voltage of a few to a few tens of micro-volts across the membrane of the bacterium for voltage-dependent cell gating [78]. Whilst the electric field shown in figure 13 may not necessarily cause direct biological effects on its own, it is possible that it may assist biological effects induced by other mechanisms [79].

The average concentrations of long-living species, such as H_{aq}^+, nitrate, nitrite, H_2O_{2aq} and O_{3aq}, are shown in figure 14, as a function of the plasma-on time. In comparison with our own experimental measurements, the numerical H_2O_{2aq} concentration is 1.3 ~ 2.2-fold higher, the nitrate/nitrite concentration 1.82-fold lower, and the O_{3aq} concentration 1.2 ~ 1.4-fold lower. Such differences between computational and
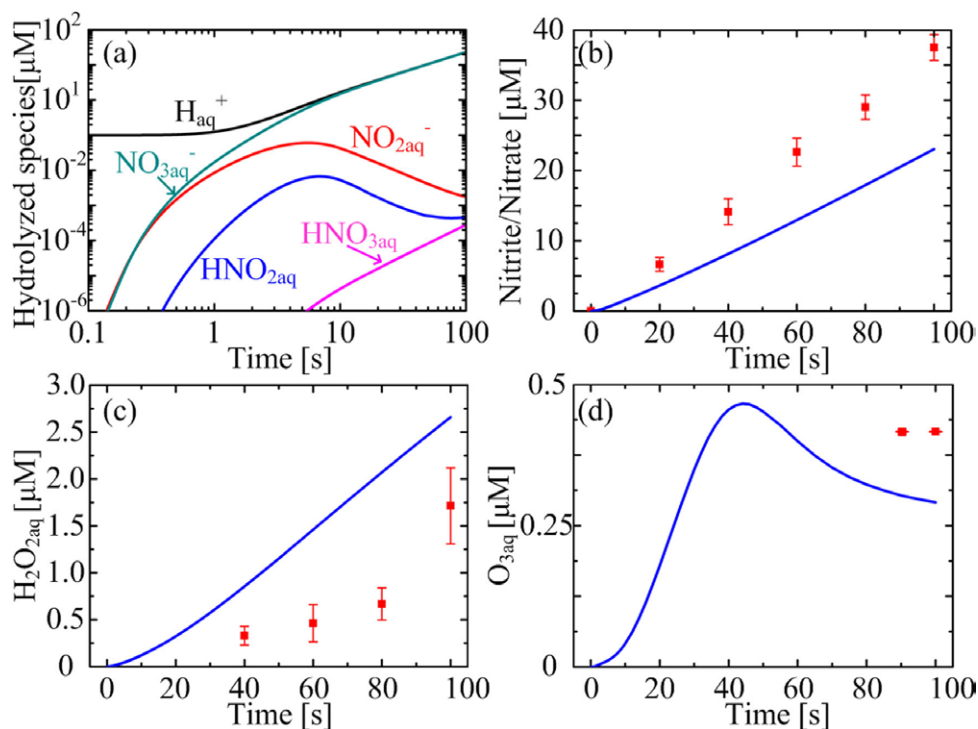
Figure 14. (a) Calculated spatial-averaged concentrations of long-living reactive species as a function of plasma treatment time SMD-treated water; and comparison with measured data for (b) nitrite/nitrate; (c) H_2O_{2aq}; and (d) O_{3aq}.

Table 6. Comparison of characteristic values of ROS/RNS in PAW and in a physiological environment.

Species	Peak density (nM)	Physiological density (nM)	Half-life (μs)	Physiological half-life (μs)
O_{2aq}^-	0.28	$0.02 - 0.2$ [84, 85]	6.11	35 [86][a]
HO_{2aq}	8.66	—	17.3	$<O_{2aq}^-$ [87]
HO_{3aq}	1.92	—	4.53	—
OH_{aq}	1.56	~zero [88]	3.19	0.001 [89]
$ONOOH_{aq}$	9.74	$2-63$ [90, 91][b]	5.19×10^5	1500 [92, 93][c]
O_2NOOH_{aq}	241	—	7.68×10^6	—
NO_{aq}	2.26×10^{-4}	$0.1-5$ [94]	8.18×10^3	$2 \times 10^3 - 2 \times 10^6$ [95]
NO_{2aq}	12.89	8×10^{-4} [86]	5.65×10^3	7 [84]
NO_{3aq}	27.44	2.1×10^{-6} [86]	1.6×10^3	—

[a] The half-life of O_{2aq}^- in a physiological environment depends on the concentration of superoxide dismutase.
[b] The density is for both the $ONOOH_{aq}$ and its hydrolyzed ion $ONOO_{aq}^-$.
[c] The half-life strongly depends on the concentration of CO_{2aq}.

experimental results are small. It is worth noting that the O_{3aq} detection limit is $0.01\,mg\,L^{-1}$ (or 208.3 nM), higher than the simulation result for $t < 30$ s, so the O_{3aq} concentration was measured at $t > 80$ s.

Our simulation suggests that the concentrations of H_{aq}^+, nitrate and H_2O_{2aq} increase with time nonlinearly in the first few seconds, but their time-dependence become almost linear after $t = 10$ s. This does not apply to nitrite and O_{3aq}, because these two species strongly react with each other (R32, appendix A), and for nitrite it is also because the ratio of $[NO_{2aq}^-]/[HNO_{2aq}]$ is strongly dependent on the pH value. At $t = 100$ s, the average density of H_{aq}^+ is 23.11 μM, and it is 2.66 μM, 2.21 nM, 23.03 μM, and 0.29 μM for H_2O_{2aq}, nitrite, nitrate and O_{3aq} respectively. Previous studies suggest that the main reactive species in the SMD-activated water are H_{aq}^+,

nitrite, nitrate, peroxynitrite and H_2O_{2aq} [76]. While this view is in general consistent with our findings, we suggest that O_{3aq} can have high concentrations and the concentrations of peroxynitrite and nitrite are likely to be lower.

The concentrations of long-living ROS/RNS are in general comparable to those reported literature, and are known to have strong biological effects. Several antibacterial mechanisms related to long-living reactive species have been proposed for the PAW. The peroxone process (R30) between O_{3aq} and H_2O_{2aq} was suggested to be the main mechanism because it can generate more reactive species like OH_{aq} and HO_{2aq} *in situ* [80]. This is true if the O_{3aq} and H_2O_{2aq} concentrations are sufficiently high. In the case of SMD as studied here, the peroxone process is not the main pathway for the generation of OH_{aq} and HO_{2aq} (see figure 11) and as such is unlikely to be important. Alternatively nitrite, nitrate, peroxynitrie and

H_2O_{2aq} are likely to be the key species, because they can serve as starting reaction partners to generate NO_{aq}, OH_{aq}, NO_{2aq} and HO_{2aq} *in situ*. The latter short-living species have strong antibacterial effect when the water is acidified [22, 76]. In contrast, the O_{3aq} concentration was found to be strongly correlated to the antibacterial efficiency without even requiring water acidification [27]. In our case, the concentration of O_{3aq} is high enough to have strong antibacterial effect alone especially for *E. coli* [81]. However this cannot be said for other species; for example, much higher H_2O_{2aq} concentration than 150 μM is needed for the deactivation of *Escherichia coli* [82]. The synergistic effect of several reactive species can enhance the antibacterial effect; for instance, a mixture of nitrite, nitrate and H_2O_{2aq} in acidified water (i.e. a high density of H_{aq}^+) has much stronger antibacterial ability than any species alone [28]. The densities of H_{aq}^+, nitrite/nitrate and H_2O_{2aq} are comparable to those in [28], so their synergy effect must be an additional mechanism to O_{3aq} for the antibacterial ability of SMD-activated water.

The antibacterial effects of long-living reactive species are therefore ultimately facilitated through their short-lived products, such as OH_{aq}, NO_{aq} and $ONOOH_{aq}$, since such species are generated *in situ* and are more cytotoxic [75, 76, 80]. Their effects may be closely linked to O_{3aq} as it leads to a chemical chain of $OH_{aq} \rightarrow HO_{2aq} \rightarrow HO_{3aq}$ as discussed above. The characteristic values of short-living species in the PAW at $t = 100$ s are listed in table 6 together with their physiological values. The concentrations of NO_{aq} and $ONOOH_{aq}$ in the PAW are either comparable to or lower than their physiological values, so these ROS/RNS species alone may have effects on cell signaling but not necessarily the more forceful effects needed for the killing of bacterial and cancer cells. For ROS, the physiological densities of OH_{aq}, O_{2aq}^-, HO_{2aq} and HO_{3aq} need to be very low due to their strong reactivity. For example, OH_{aq} is understood to react with any organic molecules and thus its diffusion length in cells is just 3 nm [83]. On the other hand, the concentrations of some RNS such as NO_{2aq} and NO_{3aq} in PAW are much higher than their physiological values by several orders of magnitude. The nitroxidative stress of these RNS is known to be lower than the oxidative stress of ROS (e.g. OH_{aq}), but is not negligible. For instance, NO_{2aq} is an initiator of lipid peroxidation [84] and has antimycobacterial effect [85]. So the NO_{2aq} and NO_{3aq} concentrations in figure 10 are not negligible.

A comparison between the half-life times of reactive species in PAW and in the physiological environment further highlights their biological importance. The differences in half-life time are obvious for the biologically effective species. Take OH_{aq} and NO_{2aq} for instance—their half-life times in PAW are higher than in the physiological environment by more than two orders of magnitude. This indicates that, if some biological substance is added into PAW, most of such reactive plasma species are likely to strongly contribute to the reactions with the biological substance. On the other hand, O_{2aq}^- and NO_{aq} are known to have modest biological effects and their half-life times in PAW are comparable to those in the physiological environment. All these short-living species

have their concentration peaks at the gas–liquid interface, except for NO_{aq} and NO_{2aq} which peak at 9.45×10^{-6} m and 5.9×10^{-6} m in the liquid (see figure 10), respectively. This indicates that the biological effect of such species may be localized in the surface layer of PAW.

The above discussion of the biological effects of these RNS and ROS is largely in reference to microorganisms, simply because most reported biological effects of plasma are for microbial inactivation. It is conceivable that other biological effects are likely to be elicited by plasma. The aqueous ROS/RNS concentrations induced by the surface plasma in figure 2 are in general low and around the physiological ROS/RNS levels. This appears to suggest that in addition to bacterial inactivation the beneficial use of the SMD may also be a trigger to manipulate some inherent biological effects or cellular functions in cells and tissues. While these are new frontiers for biology studies, the modeling framework presented here and the plasma-mediated aqueous chemistry it is unraveling offer a potentially quantitative knowledge basis to assist the design and data interpretation of such new biology investigations.

5. Concluding remarks

With the vast and growing array of plasma applications in healthcare, agriculture and pollution control, one of the most central scientific questions is the chemical identities and the dose profile of the main ROS/RNS at the sample point. Ultimately, this information will be utilized to tie the reaction and transport pathways of these aqueous ROS/RNS to the upstream electron kinetics in plasma generation to drive innovations for control strategies. A key challenge is the present lack of an integrated model for all regions of plasma-liquid interactions with good experimental validation. Here we have adapted a system science approach and developed a system-level modeling framework of indirect interactions of surface air plasma with deionized water. Supported with selected measurements of liquid-phase ROS/RNS and pH, this modeling framework has already yielded a great deal of valuable information as discussed in the present study and is expected to unravel new information in future.

For the gas buffering region of the air gap, we have shown that most short-living species such as NO, OH, O, and $O_2(a^1\Delta)$ could not survive with adequate concentrations much more than 5×10^{-3} m and that the reactive species capable of directly impacting the liquid-phase chemistry are long-living species, particularly H_2O_2, O_{3aq}, HNO_{3aq} and HNO_{2aq}. In the liquid-phase, long-living species are equally important with the dominant species being H_2O_{2aq}, O_{3aq}, nitrate, nitrite, and H_{aq}^+. While it is very ineffective to generate short-living species in the gas-phase for them to be delivered to the depth of a liquid layer, short-living species such as OH_{aq} radicals can be generated *in situ* within liquid through reactions among long-living species. Such *in situ* production of short-living aqueous species is significant in showing that plasma is capable of triggering remote actions in the form of short-living radicals and their reaction chemistry. This is achieved, for the cases discussed here, by leveraging the reactions of long-living species with water molecules, yet it is

J. Phys. D: Appl. Phys. **48** (2015) 495201

Z C Liu *et al*

possible that such leveraging capacity would extend to organic and biological molecules.

The production, loss, liquid dissolution, and transport of key long-living species have been analyzed in the gas and liquid phases. For indirect plasma-liquid interactions, mutual reactions among long-living species and their dissolution in liquid combine to dictate the chemical identity and the dose profile of aqueous ROS/RNS. Despite the minor role of short-living species, the aqueous reaction chemistry is rich in its scope for synergistic effects and enables different and possibly competing mechanisms for its impact on cells, as shown by the bacterial deactivation in plasma-activated water. A comparison ROS/RNS in PAW and under physiological conditions in terms of concentrations and half-life times shows a broad dose range of plasma-induced ROS/RNS around physiological concentrations yet with differences. This shows a clear difference from, and hence possibilities to induce novel cellular effects from, ROS/RNS produced biologically within cells and tissues. Using the example of bacterial deactivation, $O_{2\,aq}^-$, HO_{2aq}, HO_{3aq} and OH_{aq} in PAW can have strong antimicrobial effects while NO_{aq} and $ONOOH_{aq}$ may not. These will need to be clarified with future biology studies. Similarly, the biological effects of NO_{2aq} and NO_{3aq} need to be studied, as their concentrations are much higher than their physiological values.

Electric fields set up by evolving aqueous ionic species and plasma-induced acidification have been demonstrated and discussed. In general, these are modest under the conditions of our study and are unlikely to induce strong biological effects on their own. However it is plausible that they may influence cell signalling and therefore should be noted for future studies. The present study of which ROS/RNS are more important than others inevitably relies on an analysis of their concentrations and their half-life times. The finding that gas-phase plasma generation elicits liquid-phase plasma chemistry partly through remote *in situ* generation of short-living species strongly highlights that 'lesser' ROS/RNS with near-physiological-level concentrations can be important when they are placed in contact with cells that produce ROS and RNS biologically. The modeling framework presented here may have identified the difficulty for plasma-generated short-living ROS/RNS to survive their passage into any liquid layer of more than a few hundred micrometers. However it has also highlighted their *in situ* generation and the prospect of their role in modulating cell signalling. This prospect has a great deal of scope and potential for the future exploration of plasma biomedicine.

Acknowledgments

Appendix A

The aqueous chemistry induced by surface microdischarge in air.

NUM	Hydrolysis reaction	pKa/K		Ref
1	$H_2O_{aq} \leftrightarrow H_{aq}^+ + OH_{aq}^-$	13.999		[98]
2	$H_2O_{2aq} \leftrightarrow H_{aq}^+ + HO_{2aq}^-$	11.65		[98]
3	$OH_{aq} \leftrightarrow H_{aq}^+ + O_{aq}^-$	11.9		[98]
4	$HO_{2aq} \leftrightarrow H_{aq}^+ + O_{2aq}^-$	4.8		[99]
5	$ONOOH_{aq} \leftrightarrow H_{aq}^+ + ONOO_{aq}^-$	6.6		[99]
6	$O_2NOOH_{aq} \leftrightarrow H_{aq}^+ + O_2NOO_{aq}^-$	5.9		[71]
7	$HNO_{3aq} \leftrightarrow H_{aq}^+ + NO_{3aq}^-$	−1.34		[100]
8	$HNO_{2aq} \leftrightarrow H_{aq}^+ + NO_{2aq}^-$	3.4		[101]

NUM	Other reversible reaction	Forward coefficient	Backward coefficient	Ref
9	$HO_{3aq} \leftrightarrow O_{3aq}^- + H_{aq}^+$	1.4×10^5	5×10^{10}	[102]
10	$O_{aq}^- + O_{2aq} \leftrightarrow O_{3aq}^-$	3.6×10^9	3.3×10^3	[103]
11	$2NO_{2aq} \leftrightarrow N_2O_{4aq}$	4.5×10^8	6.9×10^3	[99]
12	$NO_{2aq} + NO_{aq} \leftrightarrow N_2O_{3aq}$	1.1×10^9	8.4×10^4	[99]
13	$2HNO_{2aq} \leftrightarrow NO_{aq} + NO_{2aq} (+H_2O_{aq})$	13.4	1.1×10^9	[101]
14	$ONOO_{aq}^- \leftrightarrow NO_{aq} + O_{2aq}^-$	0.020	5×10^9	[71]
15	$ONOOH_{aq} \leftrightarrow NO_{2aq} + OH_{aq}$	0.35	4.5×10^9	[71]
16	$ONOO_{aq}^- \leftrightarrow NO_{2aq} + O_{aq}^-$	10^{-6}	3.5×10^9	[71]
17	$NO_{2aq} + O_{2aq}^- \leftrightarrow O_2NOO_{aq}^-$	4.5×10^9	1.05	[71]
18	$NO_{2aq} + HO_{2aq} \leftrightarrow O_2NOOH_{aq}$	1.8×10^9	0.026	[71]
19	$2NO_{2aq}(+H_2O_{aq}) \leftrightarrow NO_{2aq}^- + NO_{3aq}^- + 2H_{aq}^+$	1×10^8	4.1×10^1	[104]
20	$O_{aq} + O_{2aq} \leftrightarrow O_{3aq}$	4.0×10^9	3.0×10^{-6}	[111]
21	$OH_{aq} + OH_{aq}^- \leftrightarrow H_2O_{aq} + O_{aq}^-$	1.3×10^{10}	1.7×10^6	[101, 105]

(*Continued*)

NUM	Irreversible reaction	Coefficient	Ref
22	$O_{3aq} + OH^-_{aq} \rightarrow O_{2aq} + HO^-_{2aq}$	40	[102]
23	$O_{3aq} + OH^-_{aq} \rightarrow O_{2aq} + HO^-_{2aq}$	70	[106]
24	$O_{3aq} + O^-_{aq} \rightarrow O^-_{2aq} + O_{2aq}$	5.0×10^9	[103]
25	$O_{3aq} + O^-_{2aq} \rightarrow O^-_{3aq} + O_{2aq}$	1.6×10^9	[102]
26	$O_{3aq} + HO^-_{2aq} \rightarrow O^-_{2aq} + O_{2aq} + OH_{aq}$	5.5×10^6	[102]
27	$O_{3aq} + OH_{aq} \rightarrow HO_{2aq} + O_{2aq}$	3×10^9	[102]
28	$O_{3aq} + HO_{2aq} \rightarrow O_{2aq} + HO_{3aq}$	5.0×10^8	[103]
29	$O_{3aq} + HO_{2aq} \rightarrow OH_{aq} + 2O_{2aq}$	1.0×10^4	[29]
30	$O_{3aq} + H_2O_{2aq} \rightarrow OH_{aq} + HO_{2aq} + O_{2aq}$	6.5×10^{-3}	[29]
31	$O_{3aq} + H_{aq} \rightarrow HO_{3aq}$	3.8×10^{10}	[103]
32	$O_{3aq} + NO^-_{2aq} \rightarrow O_{2aq} + NO^-_{3aq}$	5×10^5	[29]
33	$O^-_{3aq} (+H_2O_{aq}) \rightarrow OH_{aq} + O_{2aq} + OH^-_{aq}$	25	[102]
34	$O^-_{3aq} + OH_{aq} \rightarrow O^-_{2aq} + HO_{2aq}$	6×10^9	[102]
35	$O^-_{3aq} + OH_{aq} \rightarrow O_{3aq} + OH^-_{aq}$	2.5×10^9	[102]
36	$O^-_{3aq} + H_{aq} \rightarrow O_{2aq} + OH^-_{aq}$	1.0×10^{10}	[103]
37	$O^-_{3aq} + O^-_{aq} \rightarrow 2O^-_{2aq}$	7.0×10^8	[103]
38	$O^-_{3aq} + H^+_{aq} \rightarrow O_{2aq} + OH_{aq}$	9.0×10^{10}	[103]
39	$OH_{aq} + HO_{2aq} \rightarrow O_{2aq} + H_2O_{aq}$	7.0×10^9	[106]
40	$OH_{aq} + HO_{3aq} \rightarrow H_2O_{2aq} + O_{2aq}$	5×10^9	[29]
41	$OH_{aq} + H_2O_{2aq} \rightarrow HO_{2aq} + H_2O_{aq}$	2.7×10^7	[106]
42	$OH_{aq} + HO^-_{2aq} \rightarrow HO_{2aq} + OH^-_{aq}$	7.5×10^9	[103]
43	$OH_{aq} + O^-_{2aq} \rightarrow O_{2aq} + OH^-_{aq}$	1.0×10^{10}	[106]
44	$OH_{aq} + O^-_{aq} \rightarrow HO^-_{2aq}$	2.6×10^{10}	[29]
45	$2OH_{aq} \rightarrow H_2O_{2aq}$	5.0×10^9	[29]
46	$OH_{aq} + H_{aq} \rightarrow H_2O_{aq}$	7.0×10^9	[103]
47	$2HO_{2aq} \rightarrow H_2O_{2aq} + O_{2aq}$	8.6×10^5	[107]
48	$HO_{2aq} + O^-_{aq} \rightarrow O_{2aq} + OH^-_{aq}$	6.0×10^9	[103]
49	$HO_{2aq} + O^-_{2aq} \rightarrow HO^-_{2aq} + O_{2aq}$	8.0×10^7	[103]
50	$HO_{2aq} + O^-_{3aq} \rightarrow OH^-_{aq} + 2O_{2aq}$	6.0×10^9	[103]
51	$HO_{2aq} + HO^-_{2aq} \rightarrow OH^-_{aq} + OH_{aq} + O_{2aq}$	0.5	[103]
52	$HO_{2aq} + H_{aq} \rightarrow H_2O_{2aq}$	1.8×10^{10}	[103]
53	$HO_{2aq} + HO_{3aq} \rightarrow H_2O_{2aq} + 1.5O_{2aq}$	5×10^9	[29]
54	$HO_{2aq} + H_2O_{2aq} \rightarrow OH_{aq} + O_{2aq} + H_2O_{aq}$	0.5	[106]
55	$HO_{3aq} \rightarrow O_{2aq} + OH_{aq}$	1.1×10^5	[29]
56	$2HO_{3aq} \rightarrow H_2O_{2aq} + 2O_{2aq}$	5×10^9	[29]
57	$HO_{3aq} + O^-_{2aq} \rightarrow OH^-_{aq} + 2O_{2aq}$	1×10^{10}	[29]
58	$H_2O_{2aq} + O^-_{2aq} \rightarrow OH_{aq} + O_{2aq} + OH^-_{aq}$	0.13	[106]
59	$H_2O_{2aq} + H_{aq} \rightarrow OH_{aq} + H_2O_{aq}$	9.0×10^7	[103]
60	$O^-_{aq} + H_2O_{2aq} \rightarrow H_2O_{aq} + O^-_{2aq}$	5.0×10^7	[29]
61	$O^-_{aq} + H_{aq} \rightarrow OH^-_{aq}$	1.1×10^{10}	[103]
62	$2O^-_{aq} (+H_2O_{aq}) \rightarrow OH^-_{aq} + HO^-_{2aq}$	1.0×10^9	[103]
63	$O^-_{aq} + HO^-_{2aq} \rightarrow OH^-_{aq} + O^-_{2aq}$	4.0×10^8	[103]
64	$O^-_{aq} + O^-_{2aq} (+H_2O_{aq}) \rightarrow 2OH^-_{aq} + O_{2aq}$	6.0×10^8	[103]
65	$O^-_{aq} + H_{2aq} \rightarrow H_{aq} + OH^-_{aq}$	8.0×10^7	[103]
66	$2O^-_{2aq} (+2H_2O_{aq}) \rightarrow H_2O_{2aq} + O_{2aq} + 2OH^-_{aq}$	0.3	[106]
67	$O^-_{2aq} + H_{aq} \rightarrow HO^-_{2aq}$	1.8×10^{10}	[103]
68	$O^-_{2aq} + HO^-_{2aq} \rightarrow O^-_{aq} + O_{2aq} + OH^-_{aq}$	0.13	[103]
69	$H_{aq} + H_2O_{aq} \rightarrow H_{2aq} + OH_{aq}$	11	[103]
70	$H_{aq} + HO^-_{2aq} \rightarrow OH^-_{aq} + OH_{aq}$	9.0×10^7	[103]
71	$H_{aq} + H_{aq} \rightarrow H_{2aq}$	7.8×10^9	[103]
72	$H_{aq} + O_{2aq} \rightarrow HO_{2aq}$	2.1×10^{10}	[103]
73	$O_{aq} (+H_2O_{aq}) \rightarrow 2OH_{aq}$	50	[29]
74	$NO_{aq} + OH_{aq} \rightarrow NO^-_{2aq} + H^+_{aq}$	2×10^{10}	[106]
75	$2NO_{aq} + O_{2aq} \rightarrow 2NO_{2aq}$	2.3×10^6	[101]

(*Continued*)

NUM	Irreversible reaction	Coefficient	Ref
76	$NO_{aq} + HO_{2aq} \rightarrow ONOOH_{aq}$	3.2×10^9	[71]
77	$OH_{aq} + NO_{2aq}^- \rightarrow OH_{aq}^- + NO_{2aq}$	1×10^9	[101]
78	$OH_{aq} + HNO_{2aq} \rightarrow H_2O_{aq} + NO_{2aq}$	1×10^9	[29]
79	$OH_{aq} + HNO_{3aq} \rightarrow H_2O_{aq} + NO_{3aq}$	5.3×10^7	[107]
80	$OH_{aq} + ONOO_{aq}^- \rightarrow H_{aq}^+ + O_{2aq}^- + NO_{2aq}^-$	4×10^9	[99]
81	$OH_{aq} + ONOO_{aq}^- \rightarrow O_{2aq} + OH_{aq}^- + NO_{aq}$	4.8×10^9	[99]
82	$N_2O_{3aq} + ONOO_{aq}^- \rightarrow 2NO_{2aq} + NO_{2aq}^-$	3×10^8	[99]
83	$H_{aq}^+ + ONOOH_{aq} \rightarrow 2H_{aq}^+ + NO_{3aq}^-$	4.3	[71]
84	$ONOOH_{aq} \rightarrow H_{aq}^+ + NO_{3aq}^-$	0.9	[71]
85	$ONOO_{aq}^- \rightarrow NO_{3aq}^-$	8×10^{-6}	[71]
86	$NO_{2aq} + O_{2aq}^- \rightarrow NO_{2aq}^- + O_{2aq}$	1×10^9	[99]
87	$O_2NOO_{aq}^- \rightarrow NO_{2aq}^- + O_{2aq}$	1.35	[71]
88	$NO_{2aq} + OH_{aq} \rightarrow NO_{3aq}^- + H_{aq}^+$	1.3×10^9	[106]
89	$NO_{3aq} + HO_{2aq} \rightarrow NO_{3aq}^- + H_{aq}^+ + O_{2aq}$	4.5×10^9	[106]
90	$NO_{3aq} + O_{2aq}^- \rightarrow NO_{3aq}^- + O_{2aq}$	1×10^9	[106]
91	$NO_{3aq} + H_2O_{2aq} \rightarrow NO_{3aq}^- + HO_{2aq} + H_{aq}^+$	1×10^6	[106]
92	$NO_{3aq} + NO_{2aq}^- \rightarrow NO_{3aq}^- + NO_{2aq}$	1.2×10^9	[106]
93	$NO_{3aq} + OH_{aq}^- \rightarrow NO_{3aq}^- + OH_{aq}$	9.4×10^7	[100]
94	$N_2O_{3aq} (+OH_{aq}^-) \rightarrow 2NO_{2aq}^- + H_{aq}^+$	$2 \times 10^3 + 1 \times 10^8 [OH^-\ M]$	[99]
95	$N_2O_{4aq} (+H_2O_{aq}) \rightarrow NO_{2aq}^- + NO_{3aq}^- + 2H_{aq}^+$	1×10^3	[99]
96	$HNO_{2aq} + H_2O_{2aq} \rightarrow ONOOH_{aq} + H_2O_{aq}$	$1.4 \times 10^2 [H^+\ M]$	[70]
97	$O_2NOOH_{aq} + HNO_{2aq} \rightarrow 2H_{aq}^+ + 2NO_{3aq}^-$	12	[108]
98	$N_2O_{5aq}(+H_2O_{aq}) \rightarrow 2H_{aq}^+ + 2NO_{3aq}^-$	5×10^9	[100]
99	$H_{aq} + NO_{2aq} \rightarrow HNO_{2aq}$	1.0×10^{10}	[70]
100	$H_{aq} + N_2O_{aq} \rightarrow OH_{aq} + N_{2aq}$	2.1×10^6	[70]
101	$H_{aq} + NO_{2aq}^- \rightarrow OH_{aq}^- + NO_{aq}$	7.1×10^8	[70]
102	$NO_{2aq} + NO_{3aq} \rightarrow N_2O_{5aq}$	1.7×10^9	[109]
103	$ONOOH_{aq} + ONOO_{aq}^- \rightarrow NO_{2aq}^- + O_2NOOH_{aq}$	1.3×10^3	[120]
104	$O_2(a^1\Delta)_{aq} \rightarrow O_{2aq}$	2.5×10^5	[112]
105	$O_2(a^1\Delta)_{aq} + OH_{aq} \rightarrow O_{2aq} + OH_{aq}$	2.2×10^3	[113]
106	$O_{aq} + OH_{aq}^- \rightarrow HO_{2aq}^-$	4.2×10^8	[111]
107	$O_{aq} + H_2O_{2aq} \rightarrow OH_{aq} + HO_{2aq}$	1.6×10^9	[111]
108	$O_{aq} + HO_{2aq}^- \rightarrow OH_{aq} + O_{2aq}^-$	5.3×10^9	[111]
109	$2O_{aq} \rightarrow O_{2aq}$	2.8×10^{10}	[113]

Note: The reaction rate coefficient has a unit of s^{-1} for the single-body reactions, $M^{-1}\ s^{-1}$ for the two-body reactions and $M^{-2}\ s^{-1}$ for the three-body reactions; T_w represents the temperature of the liquid.

References

[1] Samukawa S *et al* 2012 *J. Phys. D: Appl. Phys.* **45** 253001
[2] Kong M G *et al* 2009 *New J. Phys.* **11** 115012
[3] Foster J *et al* 2012 *IEEE Trans. Plasma Sci.* **40** 1311
[4] Davide M, Jenish P, Vladimir Š and Paul M 2012 *Plasma Process. Polym.* **9** 1074–85
[5] Malik M A, Ghaffar A and Malik S A 2001 *Plasma Sources Sci. Technol.* **10** 82
[6] Noriega E, Shama G, Laca A, Diaz M and Kong M G 2011 *Food Microbiology* **28** 1293
[7] Gubkin J 1887 *Ann. Phys.* **32** 114
[8] Witzke M, Rumbach P, Go D B and Sankaran R M 2012 *J. Phys. D: Appl. Phys.* **45** 442001
[9] Bobkova E S, Smirnov S A, Zalipaeva Y V and Rybkin V V 2014 *Plasma Chem. Plasma Process.* **34** 721–43
[10] Bruggeman P and Leys C 2009 *J. Phys. D: Appl. Phys.* **42** 053001
[11] Babaeva N Y and Kushner M J 2009 *J. Phys. D: Appl. Phys.* **42** 132003

[12] Liu D X, Iza F, Wang X H, Kong M G and Rong M Z 2011 *Appl. Phys. Lett.* **98** 221501
[13] Liu D X, Bruggeman P, Iza F, Rong M Z and Kong M G 2010 *Plasma Sources Sci. Technol.* **19** 025018
[14] McKay K, Liu D X, Rong M Z, Iza F and Kong M G 2011 *Appl. Phys. Lett.* **99** 091501
[15] Tian W and Kushner M J 2014 *J. Phys. D: Appl. Phys.* **47** 165201
[16] Chen C, Liu D X, Liu Z C, Yang A J, Chen H L, Shama G and Kong M G 2014 *Plasma Chem. Plasma Process.* **34** 403–41
[17] Takeuchi N, Ishii Y and Yasuoka K 2012 *Plasma Sources Sci. Technol.* **21** 015006
[18] Dobrynin D, Arjunan K, Fridman A, Friedman G and Clyne A M 2011 *J. Phys. D: Appl. Phys.* **44** 075201
[19] Lee H W, Lee H W, Kang S K, Kim H Y, Won I H, Jeon S M and Lee J K 2013 *Plasma Sources Sci. Technol.* **22** 055008
[20] Boxhammer V, Morfill G E, Jokipii J R, Shimizu T, Klämpfl T, Li Y F, Köritzer J, Schlegel J and Zimmermann J L 2012 *New J. Phys.* **14** 113042
[21] Shibata T and Nishiyama H 2014 *J. Phys. D: Appl. Phys.* **47** 105203

[22] Oehmigen K, Hähnel M, Brandenburg R, Wilke C, Weltmann K D and von Woedtke T 2010 *Plasma Process. Polym.* **7** 250–7

[23] Lukes P, Dolezalova E, Sisrova I and Clupek M 2014 *Plasma Sources Sci. Technol.* **23** 015019

[24] Tresp H, Hammer M U, Winter J, Weltmann K D and Reuter S 2013 *J. Phys. D: Appl. Phys.* **46** 435401

[25] Zhang Q, Sun P, Feng H, Wang R, Liang Y, Zhu W, Becker K H, Zhang J and Fang J 2012 *J. Appl. Phys.* **111** 123305

[26] Oehmigen K, Wilke C, Weltmann K D and von Woedtke T 2011 *30th Int. Conf. on Phenomena in Ionic Gases (Belfast, Northern Ireland, UK, August 28–September 2)*

[27] Pavlovich M J, Chang H-W, Sakiyama Y, Clark D S and Graves D B 2013 *J. Phys. D: Appl. Phys.* **46** 145202

[28] Naitali M, Kamgang-Youbi G, Herry J M, Bellon-Fontaine M N and Brisset J L 2010 *Appl. Environ. Microbiol.* **76** 7662–4

[29] Kojtari A, Ercan U K, Smith J, Friedman G, Sensenig R B, Tyagi S, Joshi S G, Ji H-F and Brooks A D 2013 *J. Nanomed. Biother. Discov.* **4** 1000120

[30] Oehmigen K, Hoder T, Wilke C, Brandenburg R, Hähnel M, Weltmann K-D and Woedtke T V 2011 *IEEE Trans. Plasma Sci.* **39** 2646–7

[31] Xiong Z, Du T, Lu X, Cao Y and Pan Y 2011 *Appl. Phys. Lett.* **98** 221503

[32] Szili E J, Bradley J W and Short R D 2014 *J. Phys. D: Appl. Phys.* **47** 152002

[33] Sakiyama Y, Graves D B, Chang H-W, Shimizu T and Morfill G E 2012 *J. Phys. D: Appl. Phys.* **45** 425201

[34] Li D, Liu D X, Nie Q Y, Li H P, Chen H L and Kong M G 2014 *Appl. Phys. Lett.* **104** 204101

[35] Li D, Liu D, Nie Q, Xu D, Li Q and Kong M G 2014 *IEEE Trans. Plasma Sci.* **42** 2640–1

[36] Wu H, Sun P, Feng H, Zhou H, Wang R, Liang Y, Lu J, Zhu W, Zhang J and Fang J 2012 *Plasma Process. Polym.* **9** 417–24

[37] Nie Q Y, Cao Z, Ren C S, Wang D Z and Kong M G 2009 *New J. Phys.* **11** 115015

[38] Sun P P, Park C-H, Park S-J and Eden J G 2012 *IEEE Trans. Plasma Sci.* **40** 2946–50

[39] Reuter S *et al* 2012 Detection of ozone in a MHz argon plasma bullet jet *Plasma Sources Sci. Technol.* **21** 034015

[40] Sangoro J R, Iacob C, Naumov S, Valiullin R, Rexhausen H, Hunger J, Buchner R, Strehmel V, Kärger J and Kremer F 2011 *Soft Matter.* **7** 1678

[41] Roeselová M, Vieceli J, Dang L X, Garrett B C and Tobias D J 2004 *J. Am. Chem. Soc.* **126** 16308–9

[42] Vácha R, Slavíček P, Mucha M, Finlayson-Pitts B J and Jungwirth P 2004 *J. Phys. Chem.* A **108** 11573–9

[43] Lide D R and Frederikse H P R 1995 *CRC Handbook of Chemistry and Physics* 76th edn (Boca Raton, FL: CRC Press)

[44] Lee Y N and Schwartz S E 1981 *J. Phys. Chem.* A **85** 840–8

[45] Thomas K, Volz-Thomas A, Mihelcic D, Smit H G J and Kley D 1998 *J. Atmos. Chem.* **29** 17–43

[46] Schwartz S E and White W H 1981 *Adv. Environ. Sci. Eng.* **4** 1–45

[47] Fried A, Henry B E, Calvert J G and Mozurkewich M 1994 *J. Geophys. Res.* **99** 3517–32

[48] Park J Y and Lee Y N 1988 *J. Phys. Chem.* **92** 6294–302

[49] Lelieveld J and Crutzen P J 1991 *J. Atmos. Chem.* **12** 229–67

[50] Seinfeld J H 1986 *Atmospheric Chemistry and Physics of Air Pollution* (New York: Wiley)

[51] Hanson D R, Burkholder J B, Howard C J and Ravishankara A R 1992 *J. Phys. Chem.* **96** 4979–85

[52] Zhou X and Lee Y N 1992 *J. Phys. Chem.* **96** 265–72

[53] Régimbal J-M and Mozurkewich M 1997 *J. Phys. Chem.* A **101** 8822–9

[54] Stewart P S 2003 *J. Bacteriol.* **185** 1485–91

[55] Gong X, Takagi S, Huang H and Matsumoto Y 2007 *Chem. Eng. Sci.* **62** 1081–93

[56] Roots R and Okada S 1975 *Radiat. Res.* **64** 306–20

[57] Zhang J and Oloman C W 2005 *J. Appl. Electrochem.* **35** 945–53

[58] Newman J and Thomas-Alyea K E 2004 *Electrochemical Systems* (New York: Wiley)

[59] Davidson J F and Cullen M S 1957 *Trans. Inst. Chem. Eng.* **35** 55

[60] Hashitani T and Tanaka K 1983 *J. Chem. Soc. Faraday Trans.* **179** 1765–8

[61] Mertes S and Wahner A 1995 *J. Phys. Chem.* **99** 14000–6

[62] Ponche J L, George C and Mirabel P 1993 *J. Atmos. Chem.* **16** 1–21

[63] Botti H, Möller M N, Steinmann D, Nauser T, Koppenol W H, Denicola A and Radi R 2010 *J. Phys. Chem.* B **114** 16584–93

[64] Rudich Y, Talukdar R K and Ravishankara A R 1996 *J. Geophys. Res.* **101** 21023–31

[65] Liu D X, Yang A J, Wang X H, Rong M Z, Iza F and Kong M G 2012 *J. Phys. D: Appl. Phys.* **45** 305205

[66] Yang A, Rong M, Wang X, Liu D and Kong M G 2013 *J. Phys. D: Appl. Phys.* **46** 415201

[67] Fridman G, Brooks A D, Balasubramanian M, Fridman A, Gutsol A, Vasilets V N, Ayan H and Friedman G 2007 *Plasma Process. Polym.* **4** 370–5

[68] Ziuzina D, Patil S, Cullen P J, Keener K M and Bourke P 2013 *J. Appl. Microbiol.* **114** 778–87

[69] Julak J, Scholtz V, Kotucova S and Janouskova O 2012 *Phys. Med.* **28** 230–9

[70] Goldstein S, Squadrito G L, Pryor W A and Czapski G 1996 *Free Radic. Biol. Med.* **21** 965–74

[71] Goldstein S, Lind J and Merényi G 2005 *Chem. Rev.* **105** 2457–70

[72] Nizkorodov S A and Wennberg P O 2002 *J. Phys. Chem.* A **106** 855

[73] Yusupov M, Neyts E C, Simon P, Berdiyorov G, Snoeckx R, van Duin A C T and Bogaerts A 2014 *J. Phys. D: Appl. Phys.* **47** 025205

[74] Ikawa S, Kitano K and Hamaguchi S 2010 *Plasma Process. Polym.* **7** 33–42

[75] Machala Z, Tarabova B, Hensel K, Spetlikova E and Sikurova Land Lukes P 2013 *Plasma Process. Polym.* **10** 649

[76] Oehmigen K, Winter J, Hähnel M, Wilke C, Brandenburg R, Weltmann K-D and von Woedtke T 2011 *Plasma Process. Polym.* **8** 904–13

[77] Marla S S, Lee J and Groves J T 1997 *Proc. Natl Acad. Sci. USA* **94** 14243–8

[78] Schoenbach K H, Peterkin F E, Alden R W and Beebe S J 1997 *IEEE Trans. Plasma Sci.* **25** 284–92

[79] Zhang Q, Zhuang J, von Woedtke T, Kolb J F, Zhang J, Fang J and Weltmann K-D 2014 *Appl. Phys. Lett.* **105** 104103

[80] Lukes P and Locke B R 2005 *J. Phys. D: Appl. Phys.* **38** 4074–81

[81] Zorlugença B, Zorlugenç F K, Öztekin S and Evliya I B 2008 *Food Chem. Toxicol.* **46** 3593–7

[82] Imlay J A and Linn S 1986 *J. Bacteriol.* **166** 519–27

[83] Batandier C, Fontaine E, Kériel C and Leverve X M 2002 *J. Cell. Mol. Med.* **6** 175–87

[84] Halliwell B, Hu M-L, Louie S, Duvall T R, Tarkington B K, Motchnik P and Cross C E 1992 *FEBS Lett.* **313** 62–6

[85] Yu K, Mitchell C, Xing Y, Magliozzo R S, Bloom B R and Chan J 1999 *Tuber. Lung Dis.* **79** 191–8

[86] Nalwaya N and Deen W M 2003 *Chem. Res. Toxicol.* **16** 920–32

[87] Cadenas E and Davies K J A 2000 *Free Radic. Biol. Med.* **29** 222–30

J. Phys. D: Appl. Phys. **48** (2015) 495201

Z C Liu *et al*

[88] Cardoso A R, Chausse B, da Cunha F M, Luévano-Martínez L A, Marazzi T B M, Pessoa P S, Queliconi B B and Kowaltowski A J 2012 *Free Radic. Biol. Med.* **52** 2201–8

[89] Gebicki J M and Bielski B H J 1981 *J. Am. Chem. Soc.* **103** 7020–2

[90] Gutowski M and Kowalczyk S 2013 *Acta Biochim. Pol.* **60** 1–16

[91] Pryor W A 1986 *Annu. Rev. Physiol.* **48** 657–67

[92] Lim C H, Dedon P C and Deen W M 2008 *Chem. Res. Toxicol.* **21** 2134–47

[93] Chen B and Deen W M 2001 *Chem. Res. Toxicol.* **14** 135–47

[94] Romero N, Denicola A, Souza J M and Radi R 1999 *Arch. Biochem. Biophys.* **368** 23–30

[95] Lymar S V and Hurst J K 1996 *Chem. Res. Toxicol.* **9** 845–50

[96] Hall C N and Garthwaite J 2009 *Nitric Oxide* **21** 92–103

[97] Thomas D D, Liu X, Kantrow S P and Lancaster J R Jr 2001 *Proc. Natl Acad. Sci. US*A **98** 355–60

[98] Pastina B and LaVerne J A 2001 *J. Phys. Chem.* A **105** 9316–22

[99] Coddington J W, Hurst J K and Lymar S V 1999 *J. Am. Chem. Soc.* **121** 2438–43

[100] Herrmann H, Ervens B, Jacobi H-W, Wolke R, Nowacki P and Zellner R 2000 *J. Atmos. Chem.* **36** 231–84

[101] van Gils C A J, Hofmann S, Boekema B K H L, Brandenburg R and Bruggeman P J 2013 *J. Phys. D: Appl. Phys.* **46** 175203

[102] Tomiyasu H, Fukutomi H and Gordon G 1985 *Inorg. Chem.* **24** 2962–6

[103] Pastina B and LaVerne J A 2001 *J. Phys. Chem.* A **105** 9316–22

[104] Daito S, Tochikubo F and Watanabe T 2000 *Japan. J. Appl. Phys.* **39** 4914–9

[105] Mack J and Bolton J R 1999 *J. Photoch. Photobio.* A **128** 1–13

[106] Pandis S N and Seinfeld J H 1989 *J. Geophys. Res.* **94** 1105–26

[107] Barzaghi P and Herrmann H 2002 *Phys. Chem. Chem. Phys.* **4**, 3669–75

[108] Loegager T and Sehested K 1993 *J. Phys. Chem.* **97** 6664–9

[109] Katsumura Y, Jiang P Y, Nagaishi R, Oishi T, Ishigure K and Yoshida Y 1991 *J. Phys. Chem.* **95** 4435–9

[110] Molina C, Kissner R and Koppenol W H 2013 *Dalton Trans.* **42** 9898–905

[111] Knipping E M and Dabdub D 2002 *J. Geophys. Res.* **107** 4360

[112] Haag W R and Hoigné J 1986 *Environ. Sci. Technol.* **20** 341–8

[113] Schweitzer C and Schmidt R 2003 *Chem. Rev.* **103** 1685–757

[114] Barat F, Gilles L, Hickel B and Lesigne B 1971 *J. Phys. Chem.* **75** 2177–81